New Control Strategy of Battery Energy Storage System in Microgrids Integrated with Wind and Solar Power Plants

DUY QUANG NGUYEN[1,2], MINH KHOA NGO[2*]

[1]*Vinh Son - Song Hinh Hydropower Joint Stock Company, Gia Lai province, Vietnam*
[2]*Faculty of Engineering and Technology, Quy Nhon University, Gia Lai province, Vietnam*

**Corresponding author: ngominhkhoa@qnu.edu.vn*

(Received: 8 April 2025; Accepted: 22 January 2026; Published online: 10 May 2026)

ABSTRACT: The global shift toward renewable energy, particularly wind and solar, has led to the rapid growth and diversification of distributed energy resources (DERs). However, integrating these sources sustainably and efficiently presents major challenges for researchers, investors, and power system operators. Their impact on distribution grids, along with operational uncertainties and disturbances, requires a comprehensive, system-wide perspective. This study proposes targeted strategies to enhance renewable energy utilization, offering both economic and environmental benefits while maintaining technical reliability and energy security. The study develops a microgrid model that includes a solar plant, a wind farm, an energy storage system, a distribution grid, and loads. As the core component, the battery energy storage system (BESS) plays a vital role in grid stabilization, power quality enhancement, and voltage/frequency regulation through advanced control strategies. Simulation results are analyzed to assess grid performance, evaluate the influence of renewable sources, and verify the effectiveness of the BESS in maintaining stable microgrid operation under realistic operating conditions.

ABSTRAK: Peralihan global ke arah tenaga boleh diperbaharui, khususnya angin dan solar, telah membawa kepada pertumbuhan pesat serta kepelbagaian sumber tenaga teragih (DERs). Walau bagaimanapun, pengintegrasian sumber-sumber ini secara mampan dan cekap menimbulkan cabaran besar kepada para penyelidik, pelabur, dan pengendali sistem kuasa. Kesan sumber tersebut terhadap grid pengagihan, bersama-sama dengan ketidakpastian operasi dan gangguan, memerlukan perspektif menyeluruh pada skala sistem. Kajian ini mencadangkan strategi berfokus bagi meningkatkan penggunaan tenaga boleh diperbaharui, yang menawarkan manfaat ekonomi dan alam sekitar sambil mengekalkan kebolehpercayaan teknikal serta keselamatan tenaga. Kajian ini membangunkan model mikrogrid yang merangkumi loji solar, ladang angin, sistem penyimpanan tenaga, grid pengagihan, dan beban. Sebagai komponen teras, sistem penyimpanan tenaga bateri (BESS) memainkan peranan penting dalam penstabilan grid, peningkatan kualiti kuasa, serta pengawalan voltan/frekuensi melalui strategi kawalan lanjutan. Dapatan simulasi dianalisis bagi menilai prestasi grid, menilai pengaruh sumber boleh diperbaharui, dan mengesahkan keberkesanan BESS dalam mengekalkan operasi mikrogrid yang stabil pada keadaan operasi realistik.

KEYWORDS: *Battery energy storage system, Droop controller, Microgrid, Grid-following, Grid-forming.*

1. INTRODUCTION

Advances in power electronics, particularly in inverter technology, have driven major progress in electrical engineering and automation control. Renewable energy sources (RES), such as wind and solar, are increasingly deployed to replace conventional energy sources [1, 2]. Recent market trends further emphasize this global transition. In 2024, global investment in the energy transition reached USD 2.1 trillion, including USD 728 billion in renewables and USD 54 billion in energy storage systems, marking an 11% increase compared to the previous year [3]. That same year, global renewable power capacity increased by 18%, reaching 741 GW, with solar and wind accounting for the majority of newly installed capacity, solar alone representing 81% and wind 16% of the total [4]. The grid-forming inverter market is also projected to grow from USD 680 million in 2023 to USD 1,042 million by 2028, at a compound annual growth rate (CAGR) of 8.9% [5]. In parallel, battery energy storage deployment is accelerating, with 12.3 GW added in the U.S. in 2024 alone, a 33% year-over-year increase, and global lithium-ion battery demand exceeded 1 TWh [6]. These statistics underscore the urgency of developing effective control strategies for inverter-based resources and battery energy storage systems, reinforcing the study's real-world relevance. However, this transition has introduced significant challenges to power systems, particularly in distribution grids, impacting their stability and reliability. This study investigates typical fault conditions and operational scenarios in distribution networks, including both grid-connected and islanded microgrid modes. A series of simulations is conducted on RES-based microgrids using inverter control strategies such as grid-following, grid-forming, and droop control [7-10].

A microgrid is a part of the distribution grid, functioning as an independent electrical network that enables on-site power generation, connection, monitoring, and control of distributed energy resources. This configuration improves efficiency, enhances grid stability, and increases operational resilience. In recent years, many studies have focused on modeling and controlling microgrids, as well as fault management and real-time operational modeling under the uncertainty of renewable energy generation [11, 12]. Various control methods for inverters operating in grid-forming mode have been developed and are currently in use worldwide, including droop control, virtual synchronous machine (VSM), virtual oscillation control (VOC), and virtual impedance control (VIC) [13, 14]. These methods enable grid-forming inverters to support the grid through various functions, such as operating in islanded mode, ensuring synchronization with other generators, increasing system inertia, supporting primary and secondary frequency control, providing reactive power, adjusting voltage, damping frequency/angle oscillations, and enabling black-start capability. Among these methods, droop control is the most widely used and is adopted in this study. It establishes a linear relationship between frequency (or voltage) and the inverter's active (or reactive) power output. As frequency (or voltage) decreases, the inverter proportionally increases its active (or reactive) power output, and vice versa. This mechanism allows multiple inverters to share the load based on their rated capacities.

In microgrids, Battery Energy Storage Systems (BESS) play a critical role in stabilizing the grid and enhancing operational flexibility through controlled charging and discharging processes [15, 16]. Through power electronic inverters, BESS can independently and simultaneously regulate both active and reactive power, enabling functions including frequency support, voltage regulation, and power smoothing. As a result, BESS-based inverters are increasingly replacing traditional reactive power compensation devices due to their faster response and greater controllability [17].

This paper investigates the integration of wind power, solar power, and battery energy storage systems (BESS) in a distribution-level microgrid through mathematical modeling and real-world data in the MATLAB/Simulink environment. The study evaluates the role of BESS in enhancing microgrid stability and operational efficiency under both grid-connected and islanded modes. The main contributions of this paper are as follows: (i) Developing dynamic models and control strategies for wind, solar, and BESS subsystems connected to the distribution grid; (ii) Designing representative operational scenarios and fault conditions to assess microgrid performance under various disturbances; (iii) Conducting simulation-based analysis and evaluation of technical performance metrics, along with recommendations to improve microgrid operation.

Table 1. Summarizes representative studies on inverter-based microgrids and highlights the key differences and novel contributions of this paper

Study/ Ref.	**Microgrid Mode**	**RES Considered**	**BESS Role**	**Control Strategy**	**Fault Scenarios**	**Contribution Summary**
Anttila et al. (2022) [18]	Grid-connected & Islanded	General DERs	Not explicitly included	Droop, VSM, VOC, VIC (review)	✗	Review of grid-forming inverter control methods without new simulation or RES-BESS integration
Lamichhane & Adhikari (2023) [19]	Islanded	Solar + V2G	Inertia emulation via virtual synchronous machine	VSG control for frequency stability	✗	Focused on VSG-based frequency control in solar-based microgrid; lacks transient and BESS-aware studies
Elwakil et al. (2023) [20]	Islanded	PV-only	PV-inverter support	Bang-bang VSG control	✗	Fast frequency response via VSG, but no multi-source modeling or BESS involvement
Chakraborty et al. (2022) [21]	Islanded	Wind + PV	Implicit support via control strategy	μ-synthesis for robust GFL/GFM	✗	Hardware-in-loop validated robust controllers under wind and solar; no dedicated fault-ride-through modeling
Lin et al. (2022) [22]	Grid-connected	General RES	Voltage regulation via grid-forming inverter	Model-free predictive voltage control (MFPC)	✗	Improved voltage stability in low-inertia systems; lacks integrated fault and performance evaluation
This work	Grid-connected & Islanded	Solar + Wind + BESS	Full dynamic grid-forming support (frequency & voltage stabilization)	GFL, GFM + droop control with BESS PQ regulation	✓	Integrates detailed RES+BESS dynamic models; simulates realistic faults, islanding, and reconnection scenarios using MATLAB/Simulink

The remainder of this paper is organized as follows: Section 1 outlines the current state of the distribution grid, control strategies for renewable energy systems, related work, and the research objectives. Section 2 presents the mathematical models of the distribution grid, distributed generators (DGs), BESS, and microgrid components, along with simulation models developed in MATLAB/Simulink and representative operational scenarios. Section 3 presents the simulation results and evaluates the system's performance under different operating conditions. Finally, Section 4 provides the conclusions.

2. PROPOSED SYSTEM AND METHOD

2.1. DFIG-based wind turbine modeling

This study investigates and integrates a Type-3 wind turbine model, based on a Double-Fed Induction Generator (DFIG), into the microgrid simulation framework. The DFIG GE 1.5 wind turbine model, as shown in Figure 1, was studied and developed by Nicholas W. Miller and colleagues at GE Power Systems. It has been implemented in Simulink and used in simulations by researchers at IREQ, Hydro-Québec, Varennes, QC, Canada [23].

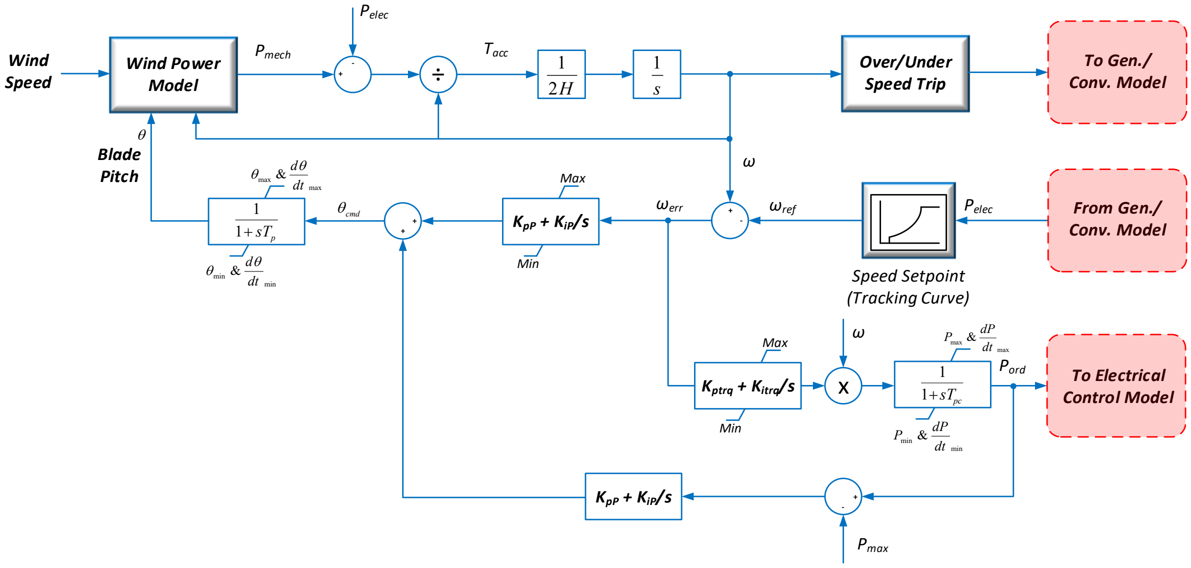

Figure 1. Dynamic modeling of a DFIG-based wind turbine.

The aerodynamic torque generated by the wind turbine is calculated as:

$$T = \frac{1}{2} C_p(\lambda, \beta)\pi\rho R^5 \frac{v_\omega^3}{\lambda^3} \tag{1}$$

where ρ is the air density (kg/m^3), R is the blade radius (m), v_ω is the wind speed (m/s), β is the blade pitch angle (degrees), and λ is the tip-speed ratio (ratio of blade tip speed to wind speed).

The power coefficient C_p, representing the wind-to-mechanical energy conversion efficiency, is given by:

$$C_p(\lambda, \beta) = 0.5176\left(\frac{116}{\lambda_i} - 0.4\beta - 5\right) e^{\frac{-21}{\lambda_i}} + 0.0068\lambda \tag{2}$$

where:

$$\frac{1}{\lambda_i} = \frac{1}{0.08\beta+\lambda} - \frac{0.035}{\beta^3+1} \tag{3}$$

The AC/DC/AC converter is divided into two main components: the rotor-side converter (C_{rotor}) and the grid-side converter (C_{grid}). Both C_{rotor} and C_{grid} are voltage source converters (VSCs) employing insulated-gate bipolar transistors (IGBTs) with forced switching to convert DC voltage into AC voltage. A capacitor, C, is connected across the DC-link, serving as a DC voltage source. Additionally, an inductor, L, is used to connect C_{grid} to the power grid [24], [25]. The three-phase rotor winding is connected to C_{rotor} via slip rings and brushes, while the stator winding is directly connected to the grid. The mechanical power captured by the wind turbine is converted into electrical power by the induction generator and delivered to the grid through the rotor and stator windings. The control system governs the wind turbine operation by generating commands for adjusting the blade pitch angle and producing control signals for the voltages V_{rc} for C_{rotor} and V_{gc} for C_{grid} to regulate the wind turbine's power, DC-link voltage, reactive power, and output voltage at the grid connection point.

In general, the absolute value of the slip coefficient s is much smaller than 1, and thus the rotor-side power P_r is significantly smaller than the stator-side power P_s. Since the mechanical torque on the rotor shaft T_m is positive for power generation, and ω_s is positive and constant due to the fixed grid frequency, the sign of P_r is a function of the slip coefficient s. P_r is positive for negative s values (i.e., when the rotor speed exceeds synchronous speed) and negative for positive s values (*i.e., when the rotor speed is below synchronous speed*). For super-synchronous operation, P_r is transmitted to the DC-link capacitor, increasing the DC voltage. For sub-synchronous operation, P_r is drawn from the DC-link capacitor and tends to decrease the DC voltage. The grid-side converter (C_{grid}) is used to either generate or absorb power (P_{gc}) to maintain a constant DC voltage. In the steady state, for a lossless AC/DC/AC converter, P_{gc} equals P_r, and the wind turbine speed is determined by the power P_r absorbed or generated by C_{rotor}. The phase sequence of the AC voltage generated by C_{rotor} is positive at sub-synchronous speeds and negative at super-synchronous speeds. The frequency of this voltage is equal to the product of the grid frequency and the absolute value of the slip. Both C_{rotor} and C_{grid} are capable of generating or absorbing reactive power and can be used to control reactive power or voltage at the grid connection point. To ensure that the DFIG operates as a generator in both modes, the power converters on both sides - the generator side and the grid side, as shown in Figure 2, must be inverters that support bidirectional power flow control. The converters enable the DFIG to operate in all four quadrants of the $P-Q$ complex plane, meaning the DFIG can supply reactive power to the grid (unlike conventional induction machines). The reactive power exchanged between the DFIG and the grid can be controlled independently of the active power [26, 27].

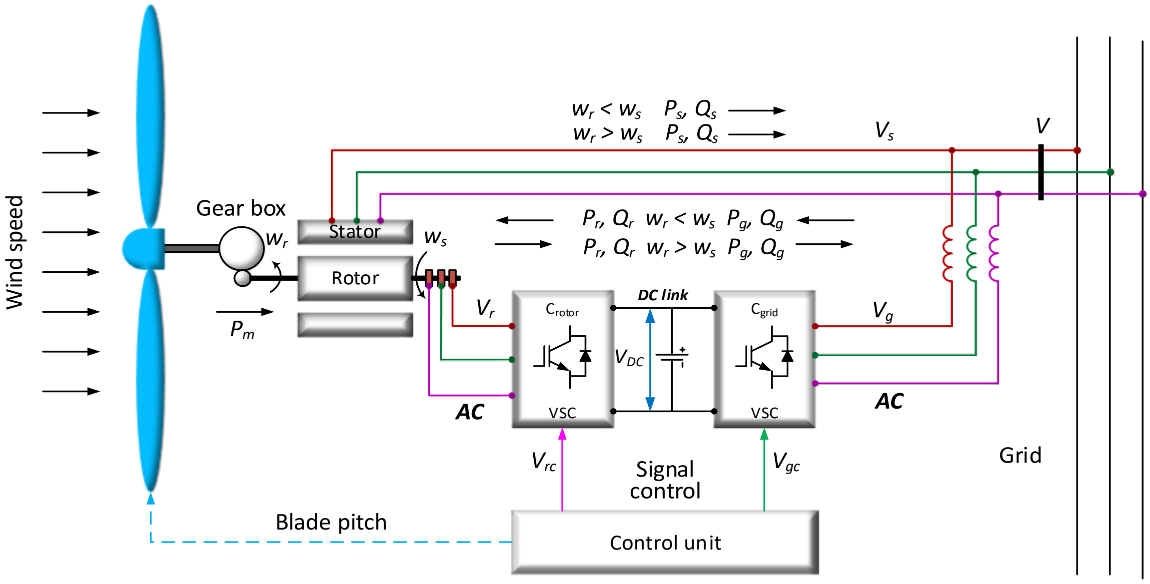

Figure 2. Control system of DFIG.

The C_{rotor} converter is used to control the wind turbine's output power and the voltage (or the reactive power) measured at the grid terminals. The actual electrical output power, measured at the wind turbine's grid terminals, is combined with the total power losses (both mechanical and electrical) and compared to the reference power obtained from the MPPT tracking characteristic. A proportional-integral (PI) controller is used to reduce the power error to zero. The output of this controller is the reference rotor current I_{qr_ref}, which must be supplied to the rotor by the C_{rotor} converter. This is the current component responsible for generating the electromagnetic torque T_{em}. The actual I_{qr} component of the positive-sequence current is compared to I_{qr_ref}, and the PI current regulator minimizes the error. The output of the current controller is the voltage V_{qr} generated by the C_{rotor}. The current controller is supported by feedforward compensation terms to predict V_{qr}. The voltage or reactive power at the grid terminals is controlled by the reactive current flowing through the C_{rotor} converter, as shown in Figure 3.

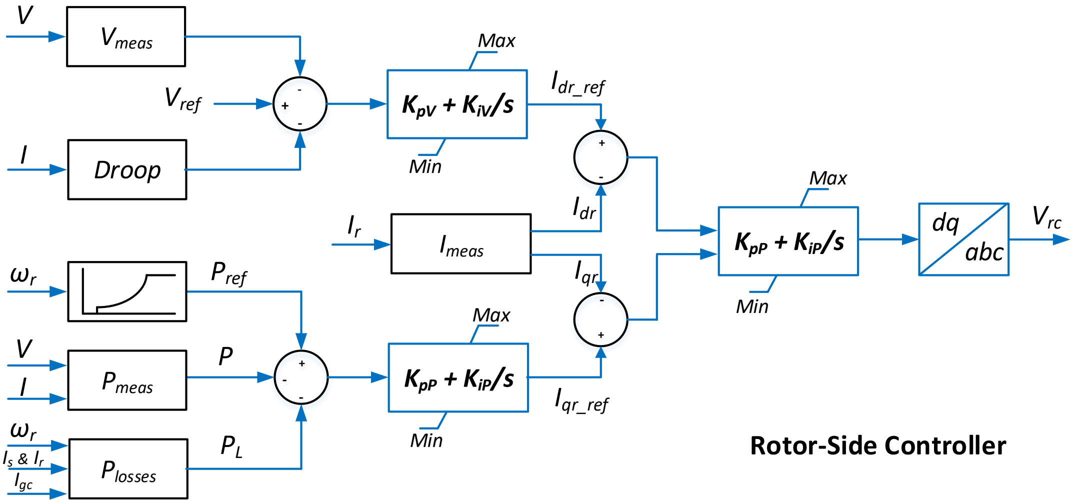

Figure 3. Rotor-side controller of DFIG.

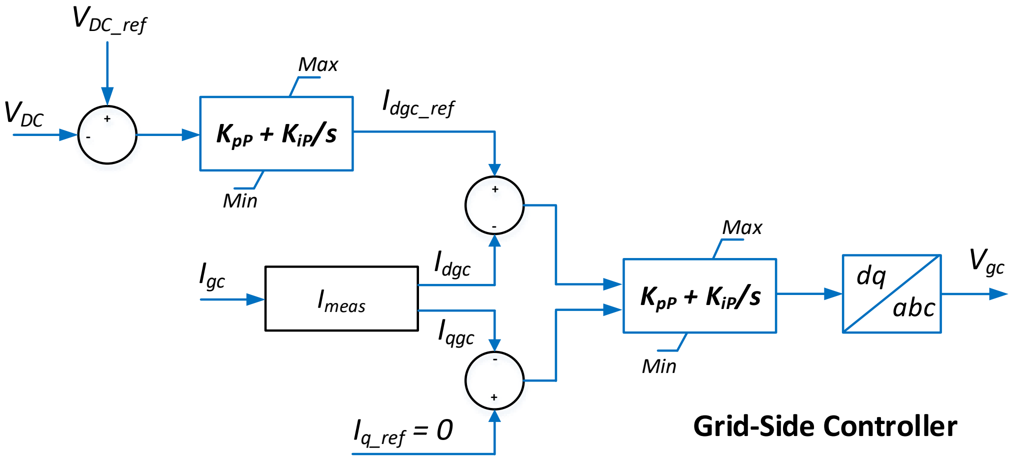

Figure 4. Grid-side controller of DFIG.

When the wind turbine operates in VAR (Volt-Ampere Reactive) control mode, the VAR controller maintains a constant reactive power at the grid terminals. The output of the voltage regulator or VAR controller is the d-axis reference current I_{dr_ref}, which must be supplied to the rotor by the C_{rotor} converter. The current regulator, similar to the power controller, is used to regulate the actual I_{dr} component of the positive-sequence current to match its reference value. The output of this regulator is the d-axis voltage V_{dr} generated by the C_{rotor} converter. The current regulator is supported by feedforward compensation terms that predict V_{dr}. The C_{grid} converter is used to regulate the DC-link capacitor voltage. Additionally, this model allows the C_{grid} converter to generate or absorb reactive power, as illustrated in Figure 4.

2.2. Solar power system modeling

Solar energy is a form of energy harnessed from sunlight and converted into electricity through photovoltaic (PV) cells. Solar power is a clean, renewable energy source that has become increasingly popular in recent years due to its numerous benefits, including reducing greenhouse gas emissions, lowering input energy costs, and enhancing energy security. Advances in science and technology have contributed to lowering the manufacturing costs of PV panels while increasing their efficiency. Additionally, modern control techniques have significantly improved the efficiency, flexibility, cost-effectiveness, and overall performance of solar power systems. Examples of such techniques include maximum power point tracking (MPPT), inverter control techniques, energy management and feedback control, and model predictive current control (MPCC) [28]. Figure 5 shows a control system of a solar power system.

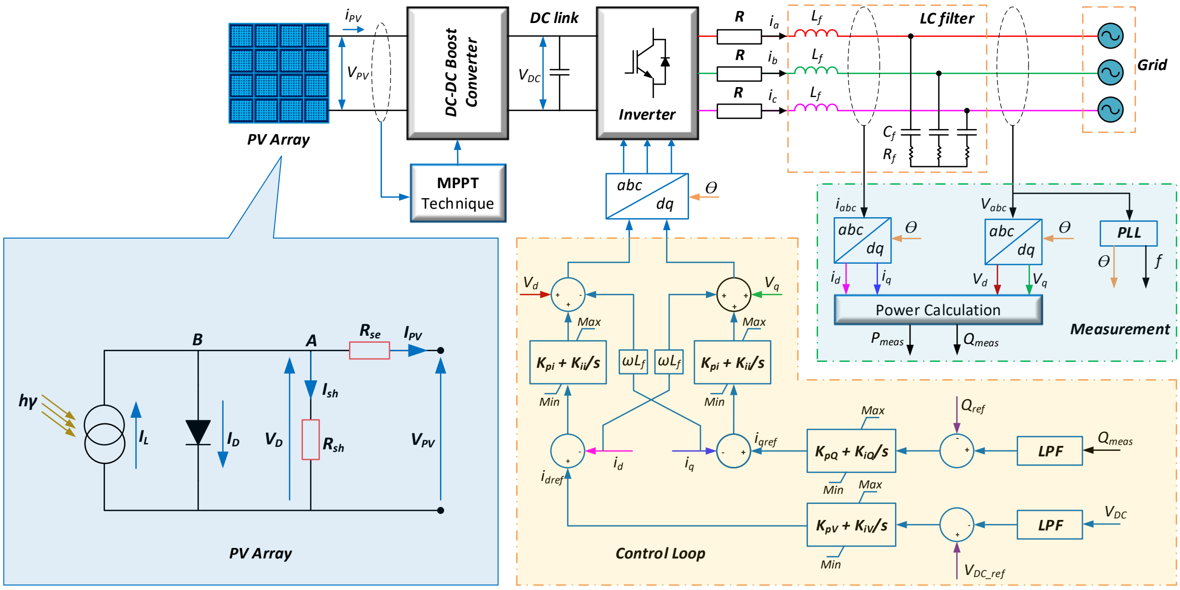

Figure 5. Control system of a solar power system.

According to Kirchhoff's current law, we have:

$$I_{PV} = I_L - I_D - I_{sh} \tag{4}$$

I_L is the photovoltaic current, independent of V_{PV} (or R_{se}), and is proportional to the incident light flux and the carrier diffusion length. It is linearly dependent on solar irradiance and also affected by temperature, as described by the following equation:

$$I_L = I_{SCr} + K_i\left(T - T_{ref}\right)\frac{G}{1000} \tag{5}$$

where I_{SCr} is the short-circuit current (under standard conditions), K_i is the short-circuit current temperature coefficient, T and T_{ref} are the operating temperature and reference temperature, respectively (in Kelvin), G is the solar irradiance on the panel surface (1000 W/m^2 is the nominal value) [28].

I_{sh} is the current flowing through the resistor R_{sh}, determined as follows:

$$I_{sh} = \frac{V_D}{R_{sh}} = \frac{V_{PV}+R_{se}I_{PV}}{R_{sh}} \tag{6}$$

I_D is the current flowing through the diode, determined as follows:

$$I_D = I_0\left(e^{\left(\frac{qV_D}{AKT}\right)} - 1\right) \tag{7}$$

where: q is the charge of an electron, $1.6.10^{-19}\text{C}$; K is the Boltzmann constant, $1.380649.10^{-23}\text{J/K}$; T is the temperature of the photovoltaic cell in Kelvin (K).

I_0 is the reverse saturation current of the diode, determined by:

$$I_0 = I_{rs}\left[\frac{T}{T_{ref}}\right]^3 \exp\left[\left(q\frac{E_{go}}{Ak}\right)\left(\frac{1}{T_{ref}} - \frac{1}{T}\right)\right] \tag{8}$$

I_{rs} is the saturation current of the diode, determined by:

$$I_{rs} = \frac{I_{SCr}}{[\exp\left(\frac{qV_{OC}}{N_S kAT}\right)-1]} \tag{9}$$

Combining equations (4), (6), and (7), we obtain the characteristic equation as follows:

$$I_{PV} = I_L - I_0\left(e^{\left(\frac{qV_D}{AKT}\right)} - 1\right) - \frac{V_{PV}+R_{se}I_{PV}}{R_{sh}} \tag{10}$$

From the characteristic equation, we can deduce:

$$I_{PV} = \frac{I_L - I_0\left(e^{\left(\frac{qV_D}{AKT}\right)}-1\right) - V_{PV}/R_{sh}}{1+(R_{se}/R_{sh})} \tag{11}$$

where A is the ideality factor of the solar cell. In the ideal case: $R_{se} \approx 0$ (ideal series resistance) and $R_{se} \sim \infty$ (ideal shunt resistance).

2.3. Battery energy storage system modeling

A battery energy storage system (BESS), as shown in Figure 6, typically consists of three main components:

- **Battery Cell Arrays:** These consist of multiple battery cells connected in series to form rows, with these rows connected in parallel to assemble a complete cluster.
- **Power Conversion System (PCS):** This is a power electronic converter responsible for inverting DC power into AC power for loads or the grid, or rectifying AC power into DC power when charging the battery array [2, 15, 29]. The PCS operates based on control signals from the control and monitoring system.
- **Control and Monitoring System:** Serving as the core of the BESS, this system adjusts voltage, frequency, changes power output, and performs functions that stabilize the microgrid.

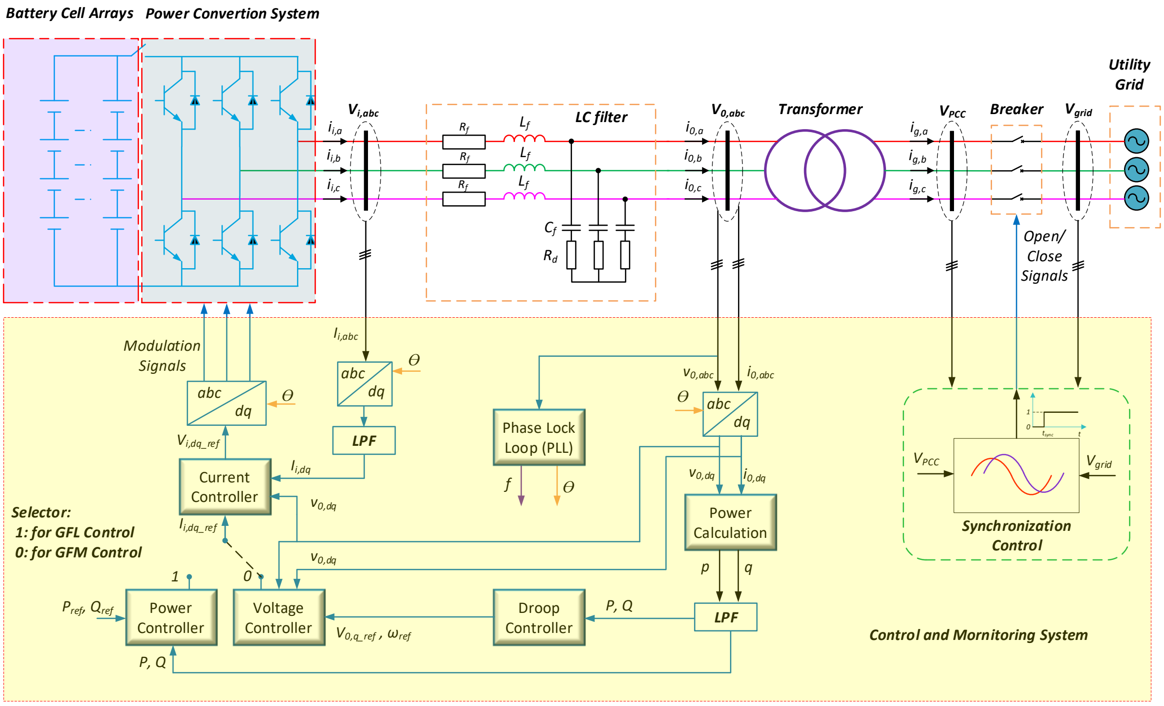

Figure 6. Control system of BESS.

The states of a battery energy storage system are defined as:

$$SoC_{min} \leq SoC(t) \leq SoC_{max} \tag{12}$$

where SoC_{max} is the fully charged state, equivalent to the rated storage capacity (C_n) and proportional to the total number of battery strings (N_b), the number of battery modules (N_{bs}), and the battery capacity (C_b).

$$C_n = C_b \left(\frac{N_b}{N_{bs}}\right) \tag{13}$$

SoC_{min} is the lowest allowable energy state of the battery energy storage system, calculated as:

$$SoC_{min} = (1 - DoD).SoC_{max} \tag{14}$$

where $DoD(\%)$ is the depth of discharge, i.e., the maximum allowable discharge percentage of the battery.

The no-load voltage of the battery (V_{nl}) is given by:

$$V_{nl} = V_0 - V_k \frac{1}{SoC} + A^{-BC_n(1-SoC)} \tag{15}$$

where V_{nl} is the no-load voltage of the battery (V), V_0 is the constant voltage of the battery (V), V_k is the polarization voltage of the battery (V), SoC is the state of charge of the battery (%), C_n is the capacity of the battery (Ah), and A, B are empirical constants.

Similar to the power converters used for distributed energy sources, the power converter of a BESS enables the conversion of active power (P) and reactive power (Q) across all four quadrants (*i.e.,* allowing independent absorption or generation of P and Q) within the rated current limits of the power electronics system.

The voltage and current values injected into the grid by the inverter are measured at the $V_{0,abc}$ node (located behind the LC filter). The three-phase voltage and current signals ($v_{0,abc}$

and $i_{0,abc}$) collected are then passed through the Park Transform block (abc/dq) to convert them into voltage and current signals in the two-dimensional dq coordinate system ($v_{0,dq}$ and $i_{0,dq}$). The instantaneous power p, q injected into the system by the BESS are calculated in the power calculation block as:

$$p = \frac{3}{2}\left(v_{0,d}i_{0,d} + v_{0,q}i_{0,q}\right) \tag{16}$$

$$q = \frac{3}{2}\left(v_{0,d}i_{0,q} - v_{0,q}i_{0,d}\right) \tag{17}$$

To obtain the average values of active power P and reactive power Q, the instantaneous values p, q must be passed through a low-pass filter (LPF), in which $LPF \rightarrow \frac{\omega_c}{s+\omega_c}$.

$$\dot{P} = -P\omega_c + \frac{3}{2}\left(v_{0,d}i_{0,d} + v_{0,q}i_{0,q}\right) \tag{18}$$

$$\dot{Q} = -Q\omega_c + \frac{3}{2}\left(v_{0,d}i_{0,q} - v_{0,q}i_{0,d}\right) \tag{19}$$

In the Grid-Following (GFL) control mode, the active and reactive powers P, Q are sent to the power controller as shown in Figure 7. Here, the calculated P, Q values are compared with the reference values P_{ref}, Q_{ref}, and the errors are processed by a proportional-integral (PI) controller. The PI controller outputs the reference control signals i_{i,d_ref} and i_{i,q_ref} for the current controller.

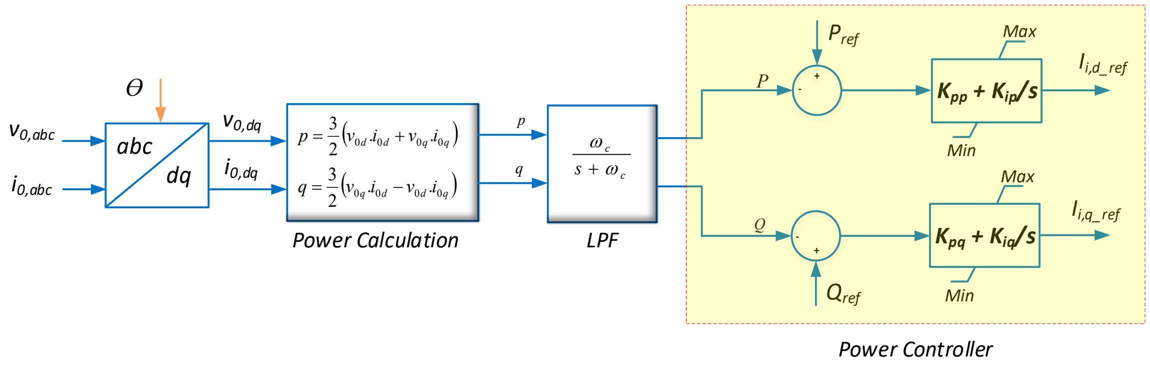

Figure 7. Power controller of BESS.

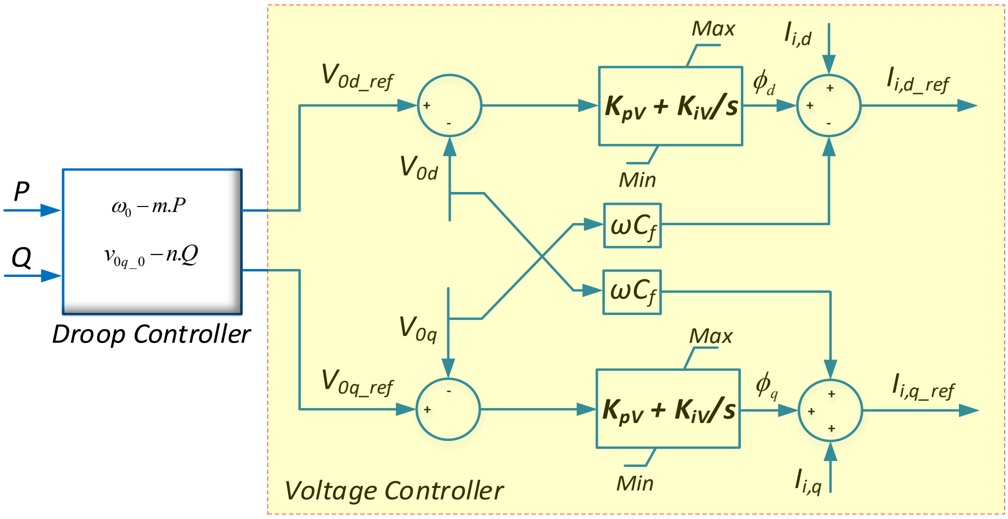

Figure 8. Voltage controller of BESS.

In the Grid-Forming (GFM) control mode, the active and reactive powers P, Q are sent to the droop controller as shown in Figure 8. Here, P, Q are referenced to calculate and output the angular frequency ω_{ref} and the reference voltage V_{0,dq_ref}, which are provided to the voltage controller. The reference voltage V_{0,dq_ref} is then compared with the measured voltage $V_{0,dq}$ at node $V_{0,abc}$, and the error is processed by a proportional-integral (PI) controller. The PI controller outputs the reference control signals $i_{i,dref}$ and $i_{i,qref}$ for the current controller.

The droop controller equations are:

$$\omega_{ref} = \omega_n - m_p(P - P_0) \text{ or } \Delta\omega_{ref} = -m_p\Delta P \tag{20}$$

$$V_{0,d\_ref} = V_{0,d_n} - n_q(Q - Q_0) \text{ or } \Delta V_{0,d\_ref} = -n_q\Delta Q \tag{21}$$

The equations of the voltage controller are:

$$\frac{d\phi_d}{dt} = v_{0,d\_ref} - v_{0,d} \tag{22}$$

$$\frac{d\phi_q}{dt} = v_{0,q\_ref} - v_{0,q} \tag{23}$$

$$i_{i,d\_ref} = i_{0,d} - \omega_n C_f v_{0,q} + K_{pv}\left(v_{0,d_{ref}} - v_{0,d}\right) + K_{iv}\phi_d \tag{24}$$

$$i_{i,q\_ref} = i_{0,q} + \omega_n C_f v_{0,d} + K_{pv}\left(v_{0,q\_ref} - v_{0,q}\right) + K_{iv}\phi_q \tag{25}$$

The inverter-side current signal (measured before the LC filter) is measured at the $V_{i,abc}$ node. This three-phase signal is transformed using the Park Transform (abc/dq) into a two-dimensional dq-axis current signal ($i_{i,dq}$), which is then passed through a low-pass filter (LPF) and sent to the current controller as shown in Figure 9. At the controller, the measured inverter current signal $i_{i,dq}$ is compared with the reference value i_{i,dq_ref} obtained from the previous control stage. The error between these values is processed by a proportional-integral (PI) controller. The reference output voltage signal v_{i,dq_ref} is determined by incorporating feedforward voltage compensation and cross-coupling compensation, where ωL_f represents the filter's equivalent reactance. This reference voltage signal is then passed through the inverse Park Transform (dq/abc) to generate the pulse modulation signals for the inverter.

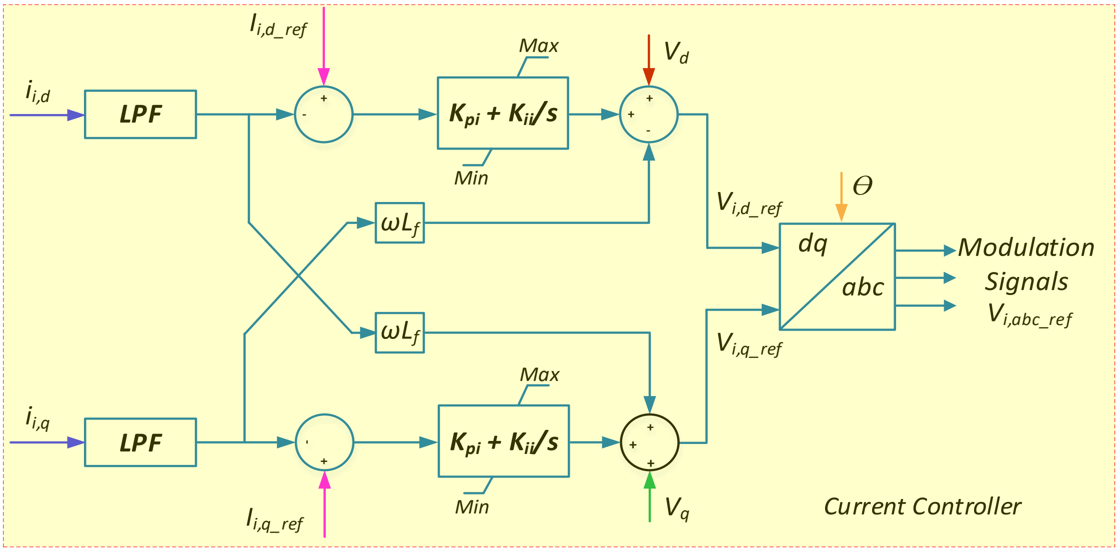

Figure 9. Current controller of BESS.

$$\frac{d\gamma_d}{dt} = i_{i,d\_ref} - i_{i,d} \tag{26}$$

$$\frac{d\gamma_q}{dt} = i_{i,q\_ref} - i_{i,q} \tag{27}$$

$$v_{i,d\_ref} = v_{0,d} - \omega_n L_f i_{i,q} + K_{pi}\left(i_{i,d\_ref} - i_{i,d}\right) + K_{ii}\gamma_d \tag{28}$$

$$v_{i,q\_ref} = v_{0,q} + \omega_n L_f i_{i,d} + K_{pi}\left(i_{i,q\_ref} - i_{i,q}\right) + K_{ii}\gamma_q \tag{29}$$

The equations of the LC filters are:

$$\frac{di_{i,d}}{dt} = -\frac{R_f}{L_f} i_{i,d} + \omega i_{i,q} + \frac{1}{L_f} v_{i,d} - \frac{1}{L_f} v_{0,d} \qquad (30$$

$$\frac{di_{i,q}}{dt} = -\frac{R_f}{L_f} i_{i,q} - \omega i_{i,d} + \frac{1}{L_f} v_{i,q} - \frac{1}{L_f} v_{0,q} \tag{31}$$

$$\frac{dv_{0,d}}{dt} = \omega v_{0,q} + \frac{1}{C_f} i_{i,d} - \frac{1}{C_f} i_{0,d} \tag{32}$$

$$\frac{dv_{0,q}}{dt} = -\omega v_{0,d} + \frac{1}{C_f} i_{i,q} - \frac{1}{C_f} i_{0,q} \tag{33}$$

2.4. Microgrid modeling

The microgrid is an integral component of the future smart grid, capable of operating autonomously in either islanded mode or grid-connected mode. In the event of a fault in the grid-connected mode, the microgrid can disconnect from the main grid and independently supply power to loads within the microgrid, as shown in Figure 10. The components of the microgrid studied in this paper include AC loads, distributed generation sources (including wind farms and solar power systems), and, notably, a battery energy storage system [11].

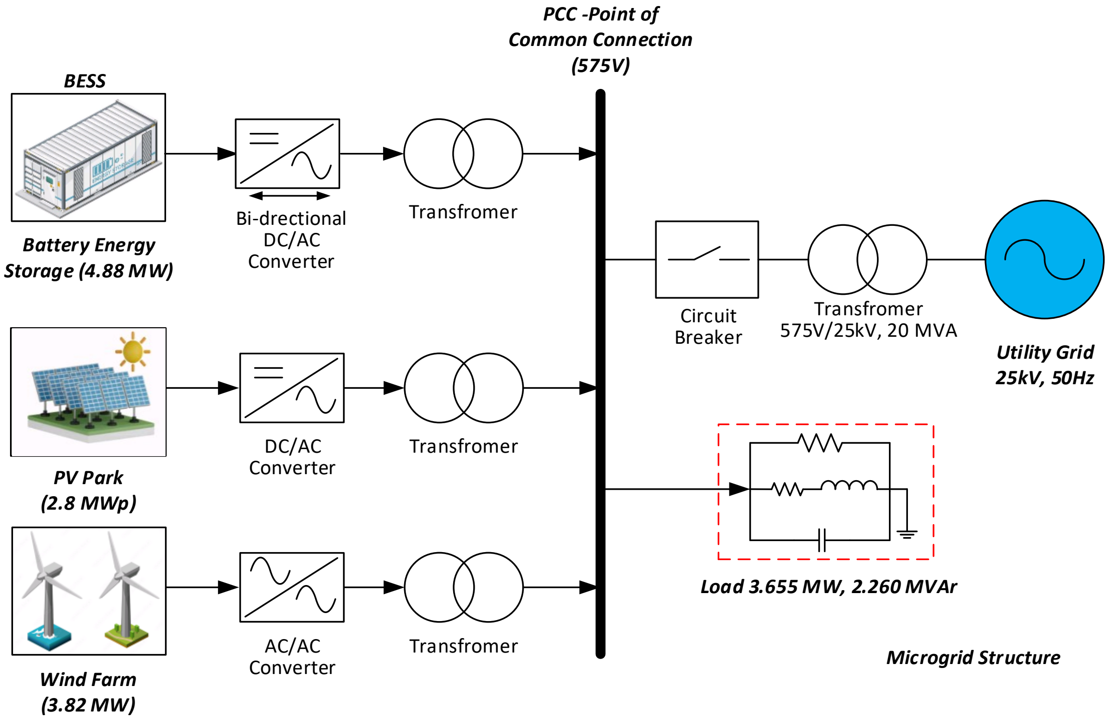

Figure 10. Microgrid structure.

The paper investigates and simulates the microgrid in two cases: grid-connected mode and islanded modes, corresponding to different scenarios, to evaluate the control performance of inverters for both the grid-following and grid-forming functions of the BESS in stabilizing the microgrid. An inverter operating with a grid-following control function is treated as a controlled current source that injects current into the grid, as shown in Figure 11. The main components include an impedance connected in parallel with a current source. In grid-following mode, the inverter is synchronized with the grid voltage through a phase-locked loop (PLL). The active and reactive power injected into the grid is controlled by adjusting the reference current values I_{dq_ref}. In this mode, the inverter only controls the power output (active and reactive power) and does not participate in regulating the grid voltage or frequency.

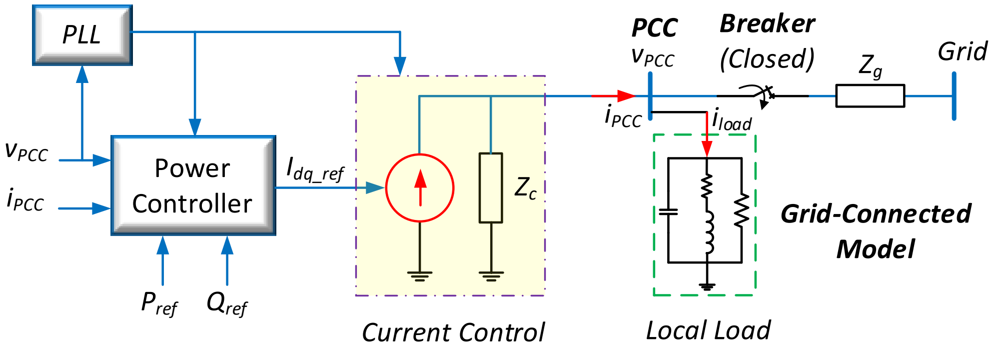

Figure 11. Grid-following control system.

In grid-connected mode, the microgrid's voltage and frequency are regulated by the synchronous generators of the main grid. However, in islanded mode, the microgrid must independently regulate its voltage and frequency to ensure stable operation, as shown in Figure 12. Unlike the grid-following control function, an inverter with grid-forming control is treated as a controlled voltage source connected in series with an output impedance, functioning similarly to a synchronous generator. In islanded mode, the inverter operates in grid-forming mode, where the voltage and frequency at the point of common coupling (PCC) are measured and compared against the reference values to control the inverter's output voltage.

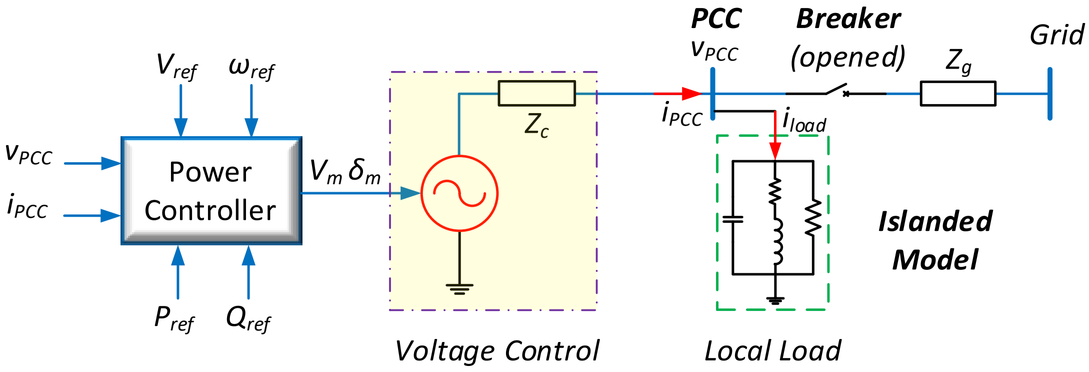

Figure 12. Grid-forming control system.

In the proposed microgrid model presented in the paper (including solar power systems, wind farms, and energy storage systems), the inverters used in the simulation include both grid-following (GFL) and grid-forming (GFM) types. Solar power systems and wind farms utilize grid-following inverters, while the energy storage system employs grid-forming inverters. This configuration accurately reflects the current state of modern power grids. Previously, the control of wind farms and solar power systems primarily focused on delivering only active power ($PF = 1$) due to the economic benefits for investors. However, the integration of BESS into the grid has become essential in both present and future contexts to ensure reliable grid operation and stability, as well as to maximize the effective utilization of renewable energy sources.

2.5. Proposed Control Strategy

The proposed control strategy distinguishes itself by integrating both grid-following (GFL) and grid-forming (GFM) inverter control modes within a unified Battery Energy Storage System (BESS) framework. This hybrid scheme enables flexible mode switching based on the grid's operational state, supporting both grid-connected and islanded operations.

Unlike conventional approaches that often regulate voltage and frequency separately, the proposed strategy enables simultaneous control of both voltage and frequency within the simulation domain, improving the microgrid's dynamic behavior during transition events such as load changes and grid reconnection. These dynamics are captured through time-based simulations to evaluate the system’s stability under varying operating conditions.

Another novel aspect lies in the integration of representative renewable energy fluctuations, including controlled PV curtailment and wind speed variations, into the simulated operational and fault scenarios. This interaction between fluctuating renewable inputs and control performance is rarely investigated in depth in previous simulation studies, as illustrated in the comparative analysis (Table 1).

Overall, this simulation-based control strategy positions the BESS not only as a stabilizing component but also as a flexible interface that enhances microgrid robustness and adaptability across diverse modeled scenarios.

3. SIMULATION RESULTS AND DISCUSSION

3.1. Case Study 1

In Case Study 1, the microgrid operates in grid-connected mode and transitions to islanded mode. The operational characteristics of the components are as follows: the solar power source generates a fixed power of $2.8\,MW$, the wind power source generates a fixed power of $3.82\ MW$, the load consumes a fixed active power of $4.005\ MW$ and the reactive power of $2.31\ MVAr$, the BESS operates in grid-following mode (GFL) and transitions to grid-forming mode (GFM) before reconnecting to the grid. The simulation in Case Study 1 is conducted over a 10-second period in Simulink, using the specified parameters. The input data for the distributed generation sources (wind and solar) and load power are as specified above. At $t = 1\ s$, a transient fault occurs on the transmission line, and the microgrid begins operating in islanded mode. Once the transient fault is cleared, the microgrid is commanded to reconnect to the grid at $t = 5\ s$. The circuit breaker is reclosed at $t = 8\ s$.

From Figure 13, we can see the microgrid power graph for Case Study 1. At $t = 1\ s$, the microgrid begins to transition to islanded mode, causing transient power fluctuations as the system changes state. The BESS starts absorbing power (i.e., enters the charging state) to balance the grid's power, and the power flow through the PCC becomes zero from this point onward. The load power slightly decreases compared to the pre-islanding stage, as the microgrid no longer exports power to the main grid via the PCC, resulting in a voltage drop within the microgrid. The power output of other distributed generation sources remains nearly unchanged after approximately two seconds of oscillation. At $t = 5\ s$, when the command to reconnect to the grid is issued, the BESS also begins to adjust the voltage magnitude, frequency, and phase angle to synchronize with the main grid. Consequently, the BESS's reactive power output increases to compensate for the voltage deficit that occurred during islanded operation.

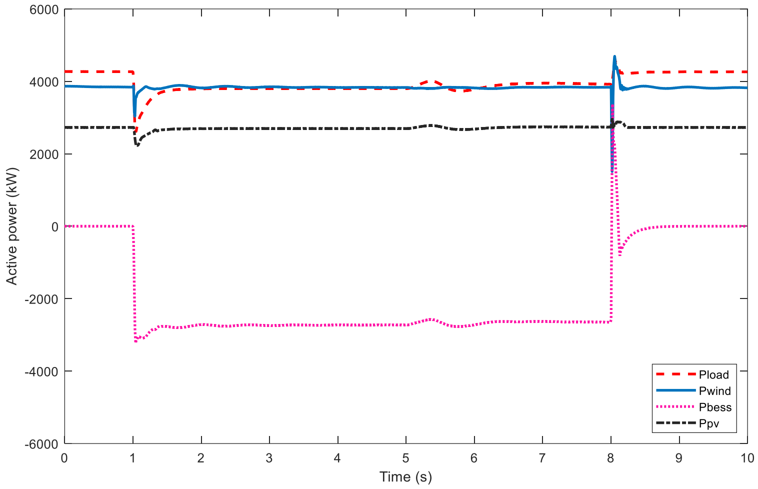

Figure 13. The active powers of the Case Study 1.

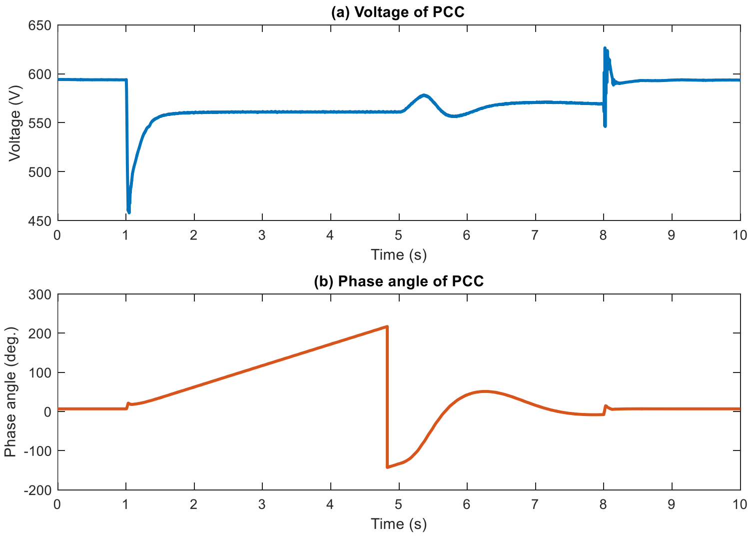

Figure 14. The voltage and phase angle at the PCC of Case Study 1.

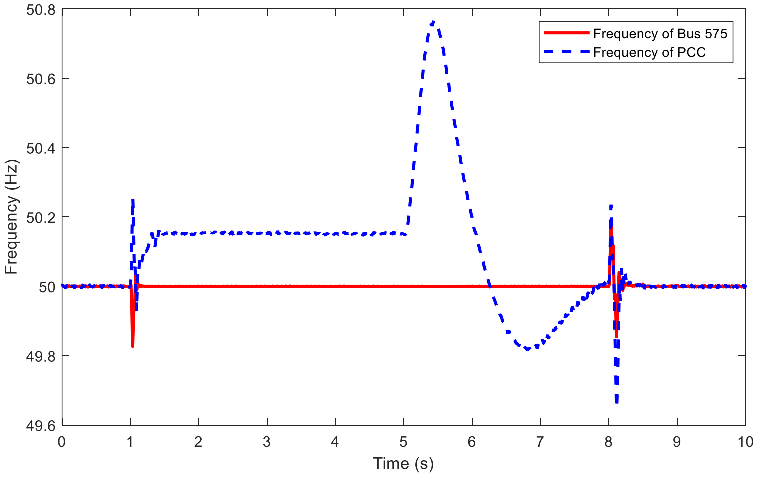

Figure 15. The frequency of the PCC and bus 575 in Case Study 1.

From Figures 14 and 15, it is easy to observe that the voltage at the PCC node before islanding is relatively high, approximately $594\,V$, because the power generated by the distributed sources is significantly greater than the load demand, and the excess power is exported to the main grid. Within the microgrid, the frequency remains approximately $50\,Hz$, essentially unchanged, as it is maintained in grid-connected mode. Upon islanding, the microgrid frequency increases slightly to around $50.15\,Hz$ due to the surplus generation, and the voltage, maintained by the BESS, drops to about $561\,V$ owing to the droop characteristics of the BESS. At $t = 5\,s$, when the reconnection command is issued, the frequency, phase angle, and voltage begin to adjust to match the grid values ($575\,V$ and $50\,Hz$), and synchronization with the grid is completed at $t = 8\,s$.

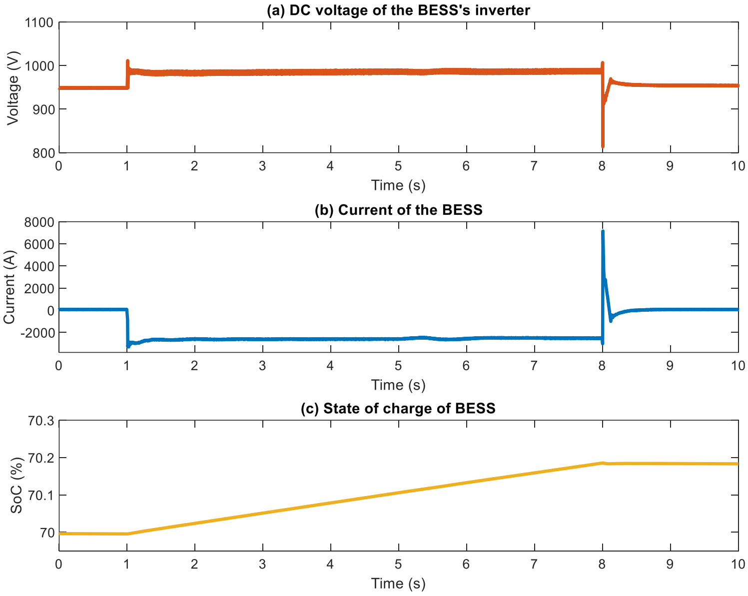

Figure 16. The BESS parameters of Case Study 1.

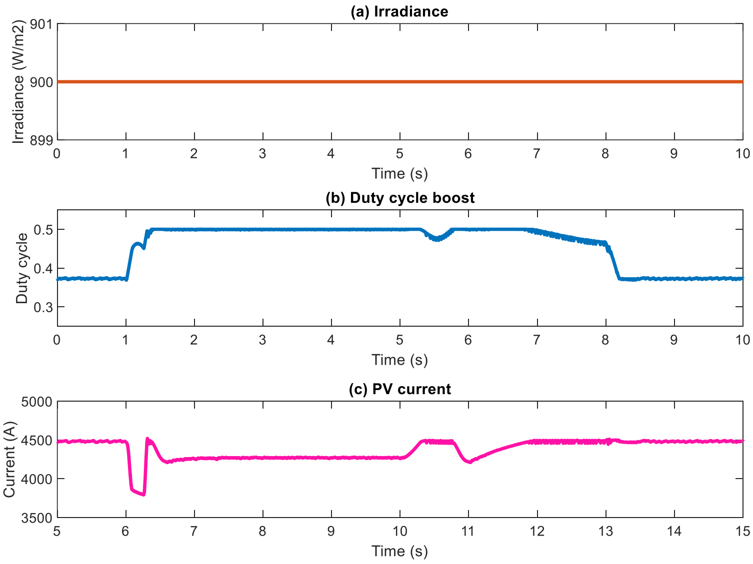

Figure 17. The solar power system parameters of Case Study 1.

The DC voltage, battery current, and state of charge (SoC) of the BESS are illustrated in Figure 16. Before the islanding event, the BESS neither absorbs nor delivers power, so its DC voltage is maintained at the nominal level (approximately 950 *V*). However, during islanding, the BESS absorbs active power, causing its DC voltage to increase slightly depending on the charging dynamics and battery characteristics (approximately 985 *V*). The battery current becomes negative during islanding because the BESS operates in charging mode, increasing its SoC during this period.

In Case Study 1, the power output of the solar and wind sources remains constant. However, the parameters of these two renewable energy sources are also affected and exhibit noticeable transient fluctuations (as detailed in Figures 16-19). In this context, the role of the BESS, specifically the grid-forming inverter, has proven effective in controlling the microgrid's voltage and frequency. This ensures the microgrid can operate independently during fault conditions and facilitates reconnection to the main grid despite fluctuations caused by integrating renewable energy sources in a weak-grid environment.

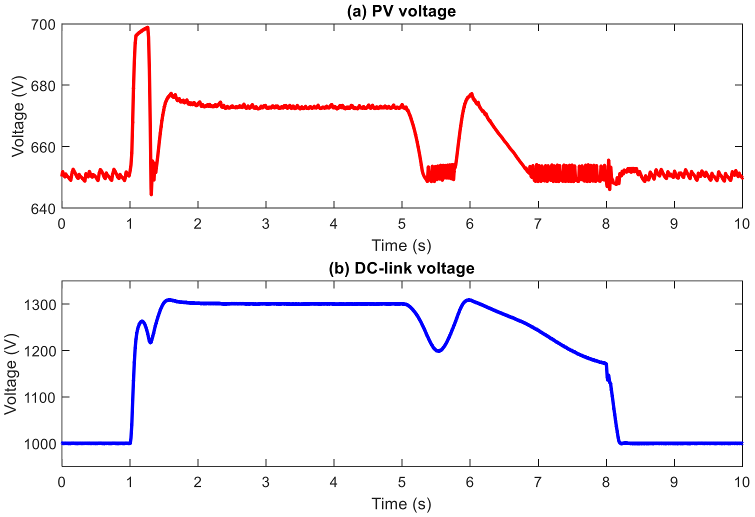
(a) PV voltage

(b) DC-link voltage

Figure 18. The solar power system parameters of Case Study 1.

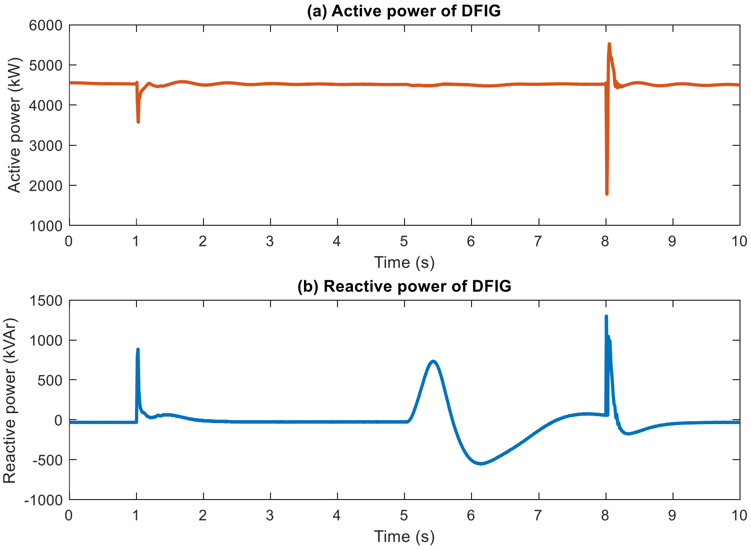
(a) Active power of DFIG

(b) Reactive power of DFIG

Figure 19. The active and reactive powers of the DFIG of Case Study 1.

In this case, the BESS, in addition to demonstrating the ability to independently and stably control the grid in islanded mode, also demonstrates enhanced dynamic performance during reconnection to the main grid while maintaining seamless grid operation. From Figures 14 and 15, it can be observed that during islanded mode, the PCC voltage is lower than the grid voltage

(561, cap V), and the frequency is slightly higher than the nominal grid frequency (50.15, cap Hz). However, when reconnection to the main grid is required, the BESS gradually adjusts these parameters toward the nominal grid values (575 V, 50 Hz) by actively regulating PQ exchange, as illustrated in Figure 14. This control capability is achieved despite the continuous fluctuations in the output parameters of the renewable energy sources during the grid synchronization phase (as shown in Figures 17-20).

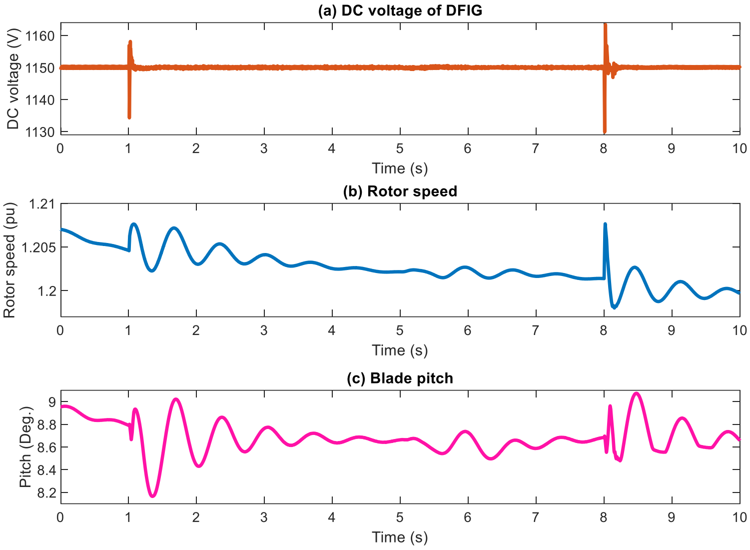

Figure 20. The DFIG parameters of Case Study 1.

3.2. Case Study 2

In Case Study 2, the microgrid operates in islanded mode, with the operating characteristics of the components as follows: the solar power source is controlled to vary its output power, the wind power source output fluctuates due to changes in wind speed, and the load consumes a constant power of 4.005 MW and 2.31 $MVAr$, the BESS operates in grid-forming mode (GFM). The input data for the output power of distributed generation sources (wind and solar) and the load power are as mentioned above. At $t = 1\ s$, the circuit breaker trips, and the microgrid transitions to islanded mode. During the islanded operation, the power outputs of distributed generation sources will fluctuate. For the solar power source, the initial output power is 2.8 MW; at $t = 3\ s$, it is reduced to 1 MW; at $t = 5\ s$, it drops to zero (0 MW), and at $t = 7\ s$, it increases again to 2 MW. For the wind power source, the initial wind speed is 15 m/s; at $t = 2\ s$, the wind speed decreases to 6 m/s, and at $t = 7\ s$, it rises to 12 m/s. To fully evaluate the functionality of BESS and the grid-forming inverter, Case Study 2 extends the analysis beyond Case Study 1 by examining additional operating scenarios of the grid-forming inverter. While the output power of renewable energy sources fluctuates in grid-connected mode, the BESS operates only in grid-following mode. In this case, the BESS assumes the grid-forming role within the microgrid to ensure stable operation. As shown in Figure 21, the microgrid power graph for Case Study 2 is illustrated. During the simulation of Case Study 2, after transitioning to islanded mode, the BESS participates in both absorbing and injecting active and reactive power to maintain the microgrid's frequency and voltage within permissible limits.

The steady-state voltage at the PCC node (Figure 22) during the islanded operation phase fluctuates between 562 and 567 V. The voltage ripples in this phase are caused by the power control of renewable energy sources (solar power). While variations in the output power of the solar source result in significant voltage oscillations, changes in wind power output are smoother and less abrupt. This difference arises from the varying sensitivity and inherent inertia of each energy source. At $t = 7\ s$, when the output power of renewable energy sources reaches its lowest point, the transient voltage of the microgrid dips to a minimum of $550\ V$.

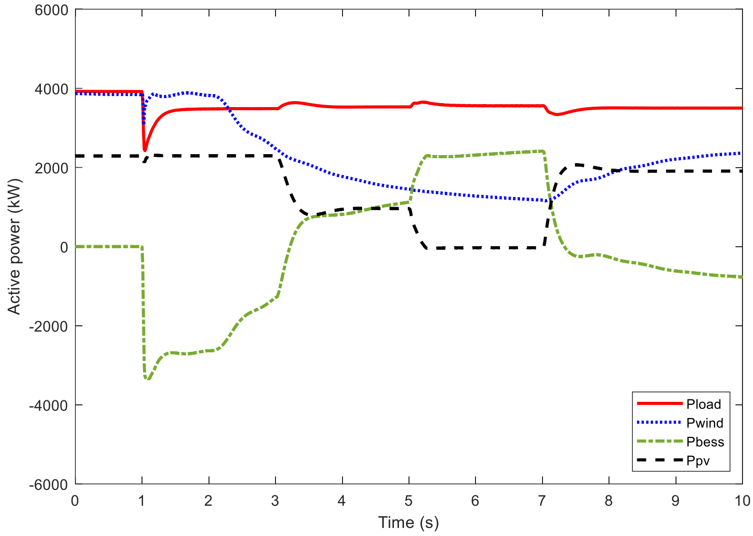

Figure 21. The active powers of Case Study 2.

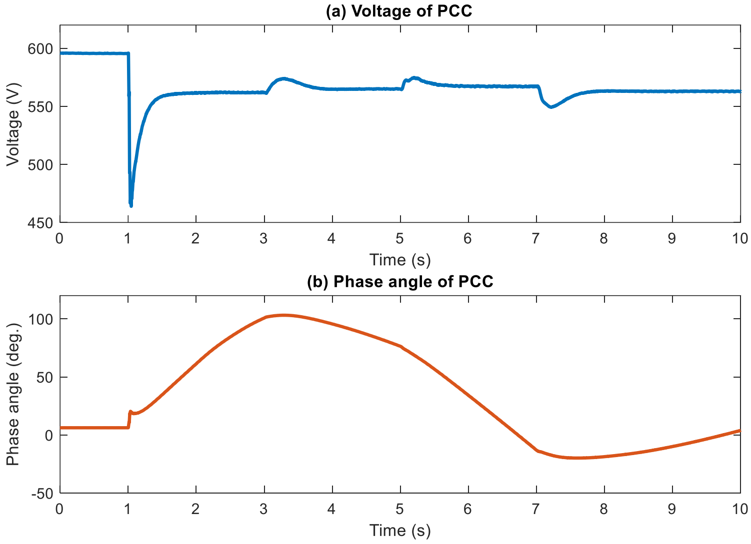

Figure 22. The voltage and phase angle at the PCC of Case Study 2.

In Figure 23, the grid frequency fluctuates within the range of $49.85 - 50.15\ Hz$ during the islanded operation phase. The frequency values accurately reflect the power output of renewable energy sources. Figure 24 illustrates the detailed parameters of the BESS under grid power fluctuations caused by renewable energy sources. The state of charge (SoC) of the battery clearly shows the alternating charging and discharging states of the BESS, which help stabilize the grid. Figures 25 and 26 depict the variations in solar power parameters under Case Study 2. In this case, the radiation value remains constant, and the solar power output is not controlled by maximum power point tracking (MPPT). Instead, it is forcibly curtailed or increased by adjusting the power control mode of the solar power control system.

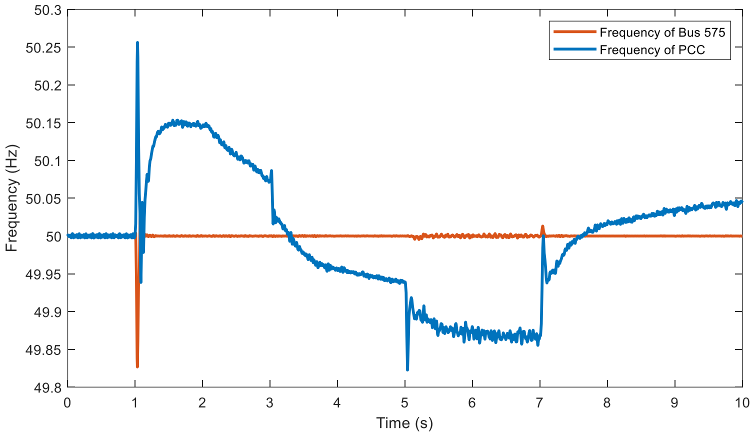

Figure 23. The frequency of the PCC and bus 575 in Case Study 2.

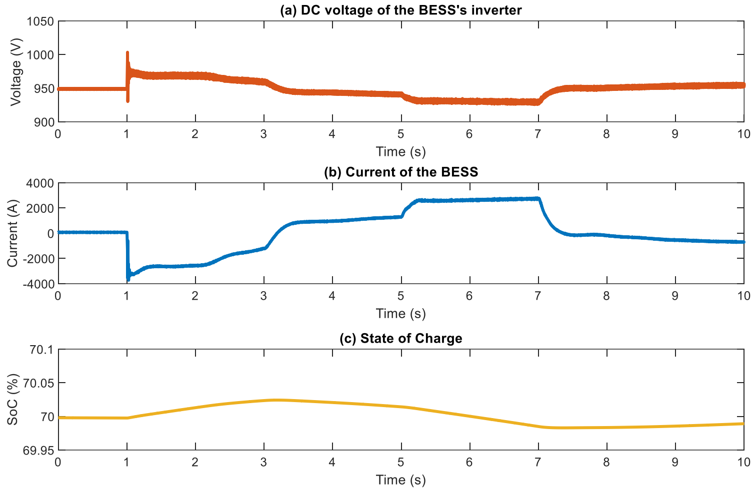

Figure 24. The BESS parameters of the Case Study 2.

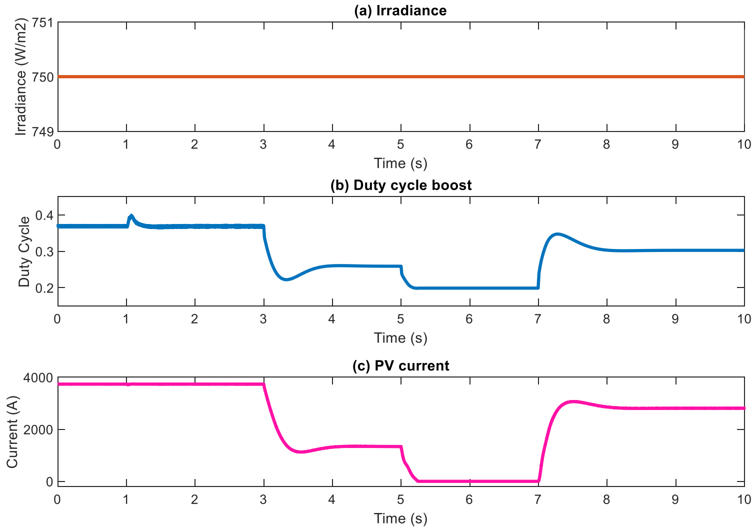

Figure 25. The solar power system parameters of Case Study 2.

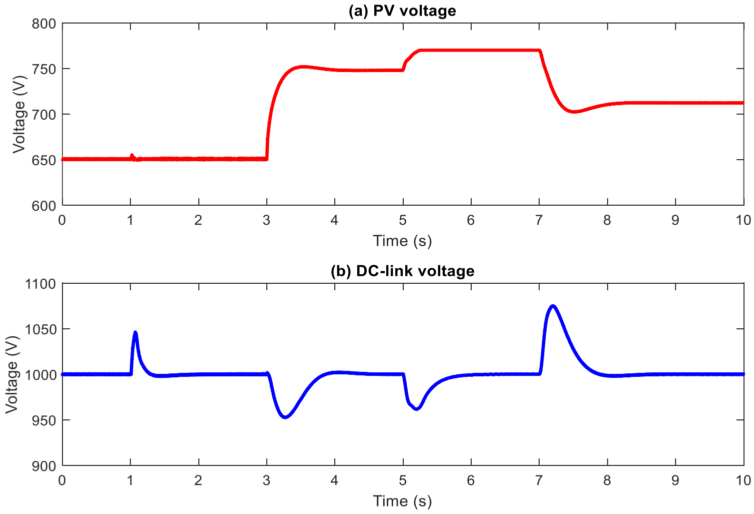

Figure 26. The solar power system parameters of the Case Study 2 (cont.)

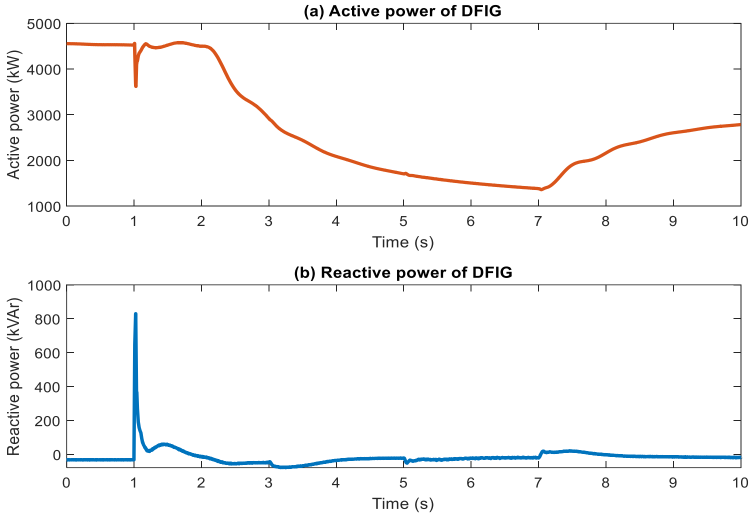

Figure 27. The active and reactive powers of the DFIG of Case Study 2.

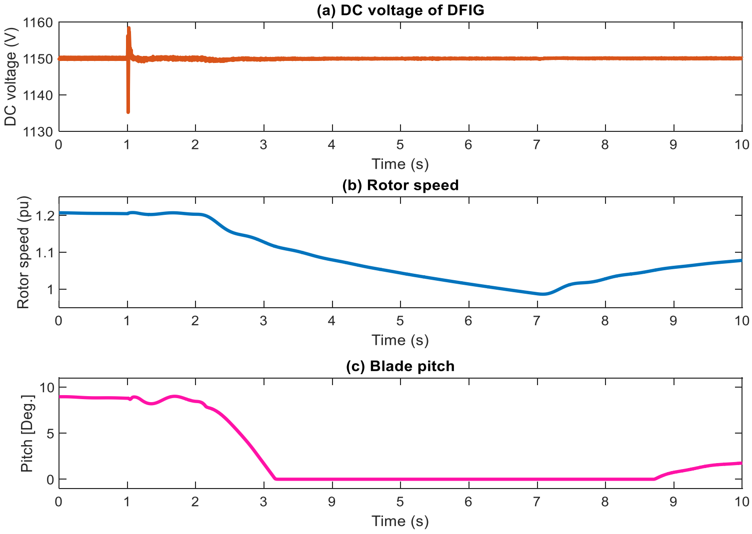

Figure 28. The DFIG parameters of Case Study 2.

Figure 28 illustrates the self-regulation behavior of power output when the wind speed drops below the rated speed. The responses of wind turbines shift to sub-synchronous operation: the wind turbine speed decreases to the rated speed (1.0 pu), and the pitch angle is controlled to zero degrees to maximize power extraction under these operating conditions. For Case Study 2, the grid operates under varying power conditions of renewable energy sources; however, in this scenario, the grid operates in islanded mode. This case demonstrates the BESS's and the grid-forming inverter's capability to stabilize the grid during islanded operation. The voltage and frequency parameters accurately reflect the performance characteristics of the droop control method.

3.3. Case Study 3

Case Study 3 involves the microgrid transitioning from grid-connected operation to islanded mode. The components exhibit the following characteristics: the solar power source produces a fixed output of 2.8 MW, the wind power generates a fixed output of 3.82 MW, the load consumes a fixed power of 4.005 MW and 2.31 $MVAr$and the BESS operates in grid-following (GFL) mode and transitions to grid-forming (GFM) mode, eventually reconnecting to the grid. Input data for distributed generation (solar and wind) and load power are as described above. At $t = 1\ s$, a fault occurs on the transmission line, causing the microgrid to switch to the islanded mode. During islanded operation, at $t = 5\ s$, a three-phase-to-ground fault transient occurs at the PCC and lasts for 8 cycles (160 ms).

Figure 29 illustrates the power dynamics in the microgrid under Case Study 3. At $t = 1\ s$, the microgrid begins islanded operation, causing power disturbances due to the state transition. The BESS starts absorbing power (i.e., enters charging mode) to balance the microgrid's power, and the power flow through the PCC becomes zero. At $t = 5\ s$, when the short circuit occurs, all components in the microgrid experience significant disturbances in power, voltage, and frequency, as detailed in Figures 30 and 31. From Figures 30 and 31, it is evident that the voltage at the PCC drops to zero during the short circuit, and the microgrid frequency undergoes large fluctuations around 50 Hz. With the BESS intervention, the microgrid voltage quickly recovers to normal and stabilizes by approximately $t = 5.4\ s$. However, wind power remains oscillatory due to wind turbine inertia, causing the microgrid frequency to continue to fluctuate. During this period, to maintain system stability, BESS adjusts its operation to compensate for variations in wind power, eventually achieving stability at $t = 9\ s$.

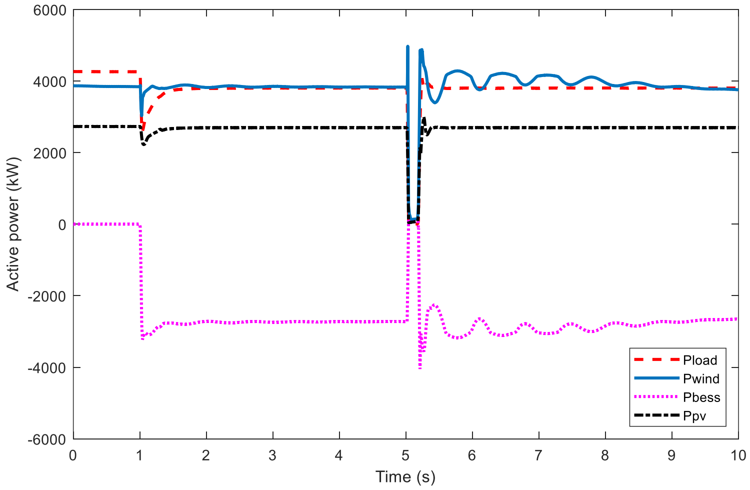

Figure 29. The active powers of the Case Study 3.

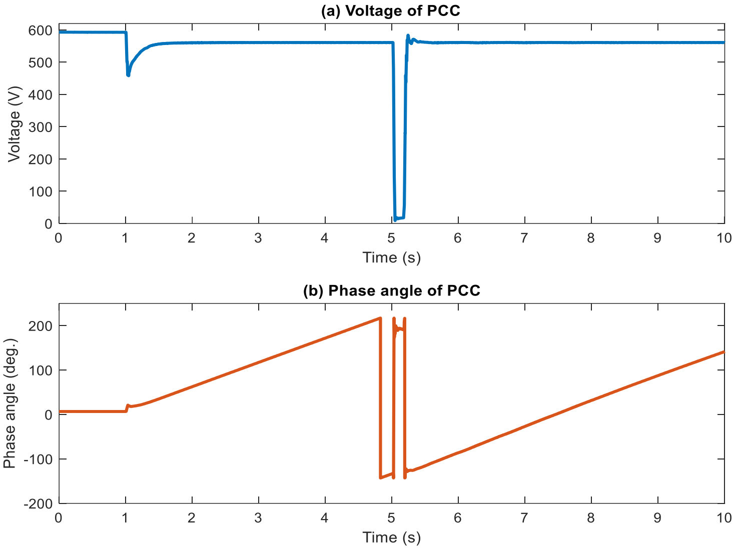

Figure 30. The voltage and phase angle at the PCC of Case Study 3.

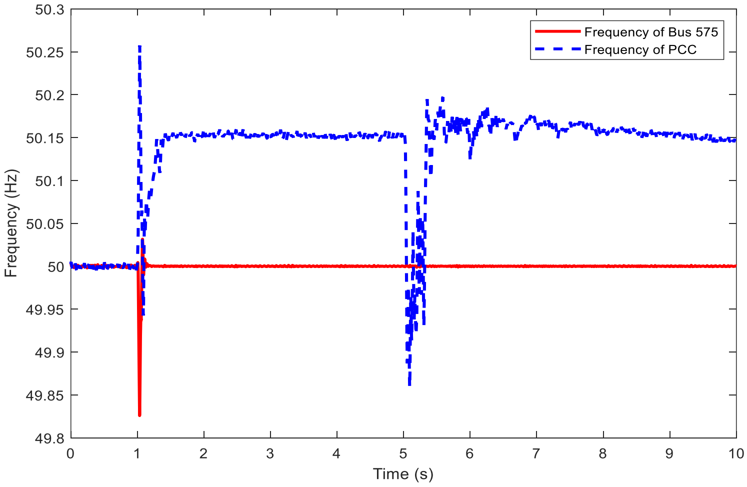

Figure 31. The frequency of the PCC and bus 575 in Case Study 3.

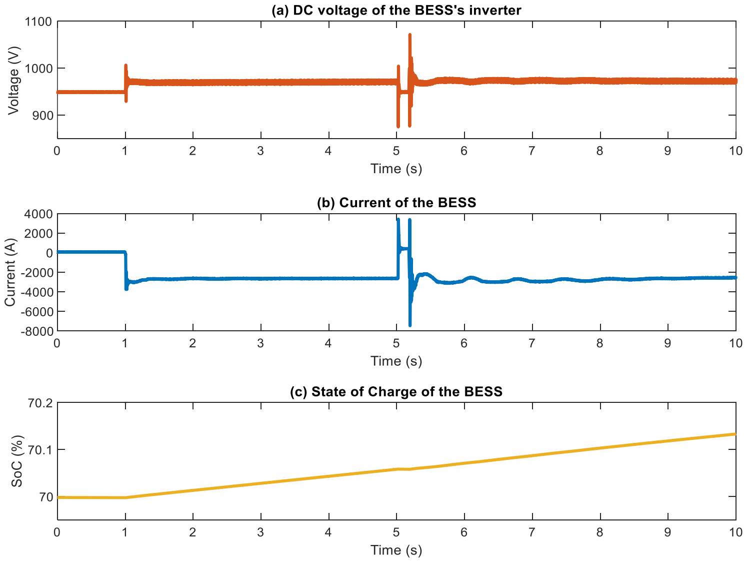

Figure 32. The BESS parameters of Case Study 3.

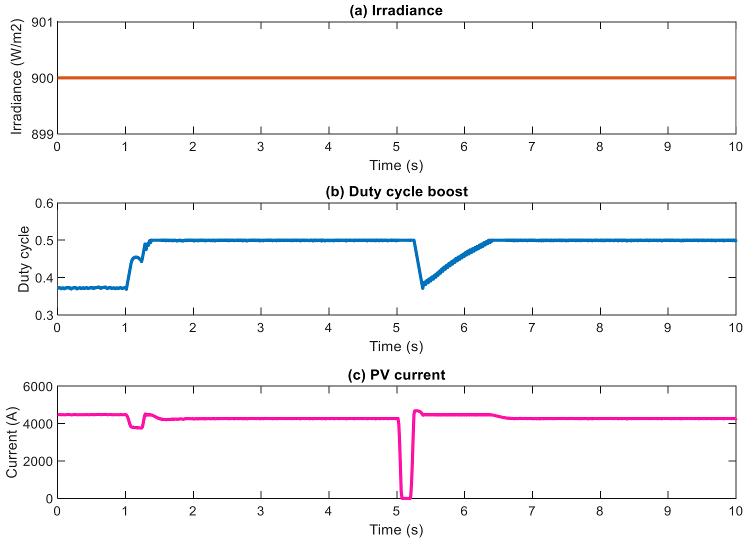

Figure 33. The solar power system parameters of Case Study 3.

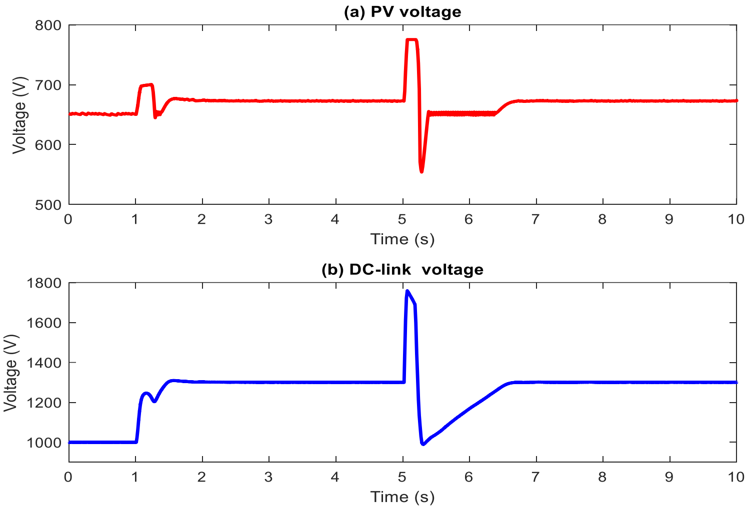

Figure 34. The solar power system parameters of the Case Study 3 (cont.)

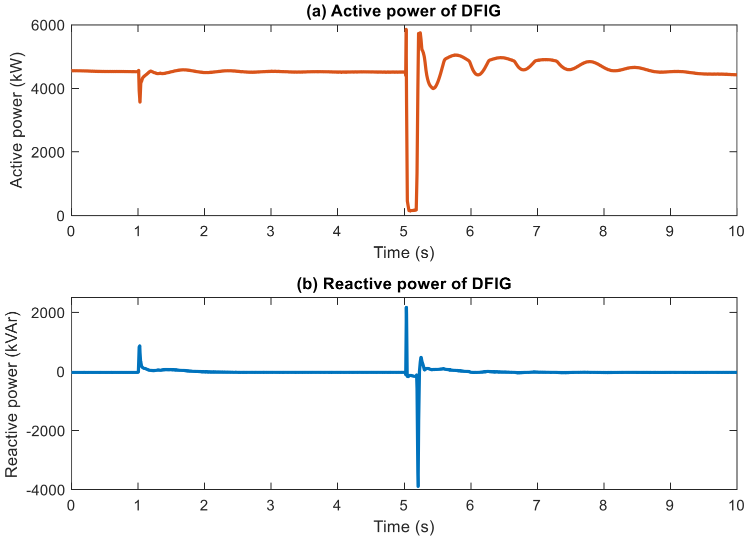

Figure 35. The active and reactive powers of the DFIG of Case Study 3.

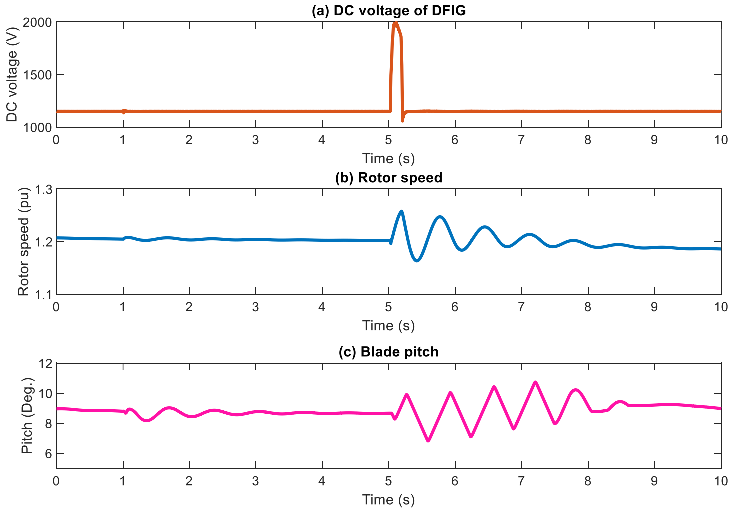

Figure 36. The DFIG parameters of Case Study 3.

From Figure 33**,** it is evident that the BESS parameters are disrupted at $t = 5\ s$ due to the fault event. However, the BESS rapidly restores stability and begins fine-tuning its control strategy after $t = 5.4\ s$. This behavior highlights the system's resilience and demonstrates the effectiveness of BESS in stabilizing the microgrid both during and after disturbances. Observing Figure 33, it can be seen that, during a fault, the photovoltaic panel current drops to zero, while the panel voltage and DC-Link voltage increase significantly. As a result, the output current of the solar power plant remains nearly unchanged, as illustrated in Figure 34 when a short circuit occurs at the Point of Common Coupling (PCC). While the parameters of solar power are only slightly affected by the short circuit at the Point of Common Coupling (PCC), the wind power output is significantly impacted, with the transient period lasting nearly 4 seconds before stabilizing, as shown in Figures 35 and 36. The prolonged transient behavior of wind power can be attributed to the wind turbine's inherent inertia and the limited response speed of the blade-pitch control system.

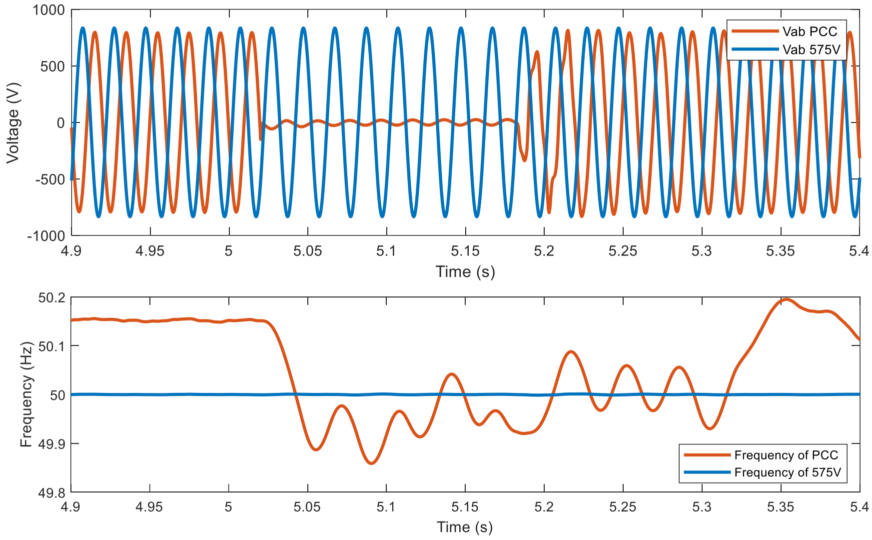

Figure 37. Voltage and frequency during a single-phase-to-ground fault.

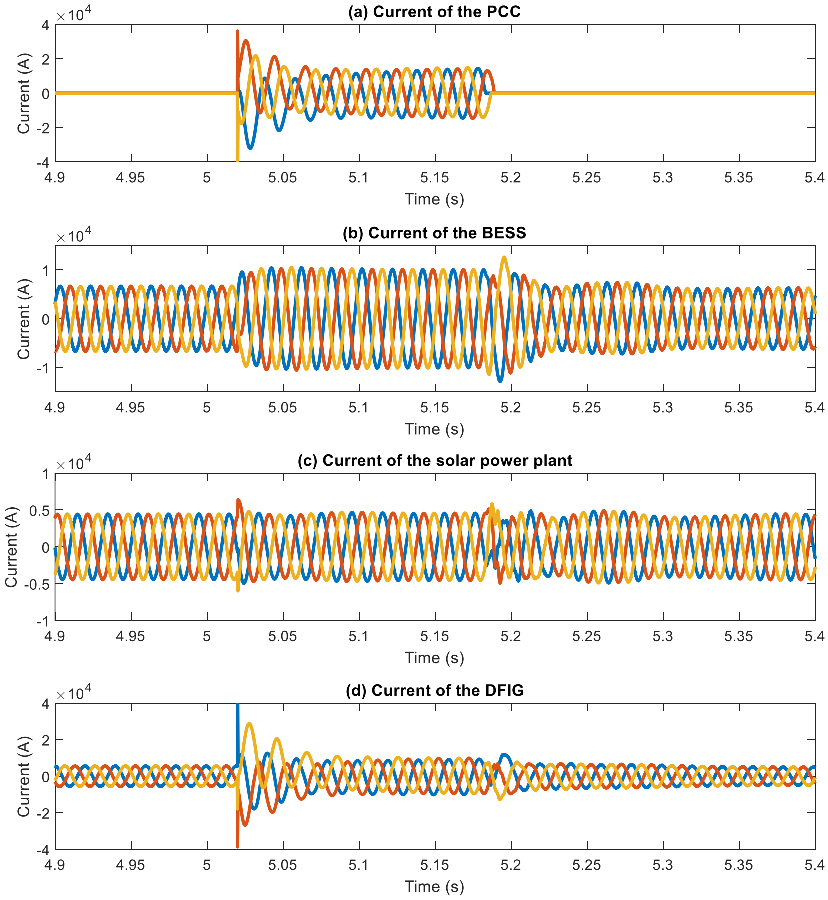

Figure 38. The current during a single-phase-to-ground fault.

Case Study 3 is an extension of Case Study 1, where the microgrid operates in islanded mode and simulates a short circuit lasting $160\,ms$ to evaluate the responsiveness of the components within the grid. The simulation also serves as a basis for calculating and configuring relay protection settings for specific cases. Based on the responses of voltage, current, and frequency, as shown in Figures 37, 38, and 39, the Fault Ride-Through (FRT) capability of the elements in the microgrid is assessed.

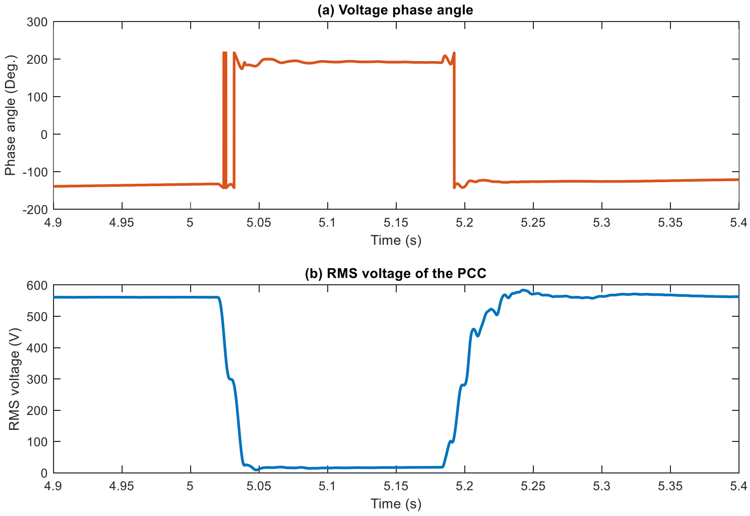

Figure 39. The voltage and phase angle at the PCC during a single-phase-to-ground fault.

Table 2. Comprehensive performance summary of case studies

Parameter	Case Study 1	Case Study 2	Case Study 3
Objective	Evaluate islanding and reconnection under GFL↔GFM transitions	Assess stability under fluctuating RES in islanded mode	Evaluate fault ride-through capability during severe disturbances
Simulation Duration	10 s	10 s	10 s
Operation Mode	Grid-connected → Islanded → Reconnected	Grid-connected → Islanded (off-grid)	Grid-connected → Islanded with faults
Type of Disturbance	Manual islanding and reconnection	RES power fluctuation (PV, wind)	Three-phase-to-ground fault
BESS Mode	GFL → GFM → GFL	GFL → GFM	GFL → GFM
Main Control Strategy	Droop + synchronization	Droop + dynamic charge/discharge	Droop + FRT voltage restoration
Solar Power	2.8 MW (constant)	2.8 → 1 MW (t = 3s) → 0 MW (t = 5s) → 2 MW (t = 7s)	2.8 MW (constant)
Wind Power	3.82 MW (constant)	15 → 6 m/s (t = 2s) → 12 m/s (t = 7s)	3.82 MW (constant)
Load Demand	4.005 MW + 2.31 MVAr	4.005 MW + 2.31 MVAr	4.005 MW + 2.31 MVAr
Voltage at PCC	561 V (steady-state) and 556-578 V (during resynchronization)	562–567 V (steady state) and 550–575 V for voltage ripple during PV power changes.	0 V for an 8-cycle fault from t = 5 s, restored at t ≈ 5.4 s
Frequency at PCC	50.15 Hz (steady-state) 49.82-50.75 Hz (during resynchronization)	49.85 – 50.15 Hz	49.85 – 50.15 Hz
Voltage Recovery Time	3 s (during resynchronization)	Approximately 1 s for ripple (after each PV power drop)	Approximately 0.2s (after fault cleared)
Frequency Recovery Time	3 s (during resynchronization)	Due to RES power variations (wind and PV), the frequency fluctuates slightly; following a sudden PV power drop, recovery occurs within approximately 0.1–0.2 s.	Approximately 3.5–4 s (due to wind power inertia)
Reactive Power Behavior (Q)	Q injection for islanding	Dynamic Q fluctuation with P changes due to RES curtailments	Q distorted during fault, then stabilizes
SoC Behavior of BESS	Increase during islanded charging	Charging/discharging dynamically	interrupts during fault, then recharges
Stability Behavior	Smooth transition, damped oscillations	Stable, fast damping after disturbances	Slow recovery, affected by RES inertia
Synchronization Behavior	Successful and seamless	N/A	N/A
Grid Reconnection Time	From t = 5 s to t = 8 s	N/A	N/A
FRT Capability Shown	N/A	N/A	Full recovery from 0 V fault
BESS Action	Absorbs surplus power (charging) and supports Q	Maintains voltage and frequency dynamically	Provides voltage and frequency recovery
Impact of BESS	Ensures reconnection and stability	Maintains operation under severe RES changes	Enables recovery from major faults
Key Observation	Smooth GFL↔GFM transitions with reconnection	Effective GFM control under dynamic RES	Supports FRT and recovers grid stability

The comprehensive performance summary of case studies is shown in Table 2. Based on the comparative results, the BESS plays a vital role in enhancing grid stability across different operating conditions. In Case Study 1, the system achieves smooth GFL↔GFM transitions with successful reconnection, although the recovery time for voltage and frequency is relatively long. In Case Study 2, the BESS demonstrates strong dynamic performance under fluctuating RES conditions, with rapid voltage and frequency recovery within 0.1–0.2 s following sudden PV drops. This indicates the effectiveness of the droop control combined with dynamic charge/discharge. In Case Study 3, the BESS enables fault ride-through capability, restoring voltage in about 0.2 s, though frequency recovery is slower due to wind inertia. Each case highlights a different strength: reconnection support, dynamic stability, and fault tolerance. Overall, the results confirm that GFM-based BESS control significantly improves system resilience and operational flexibility.

4. CONCLUSIONS

Based on the simulation results, this paper presents a comprehensive overview of power grid operation with integrated renewable energy sources and highlights the critical role, benefits, and control strategies of Battery Energy Storage Systems (BESS) in microgrids. The study provides a detailed comparison between grid-connected and islanded microgrid operation modes, investigates both grid-following and grid-forming inverter control strategies, and analyzes the impacts of disturbances and fluctuations in distributed energy resources (DERs), particularly solar and wind generation. The findings demonstrate the effectiveness of BESS in stabilizing key grid parameters and maintaining system operation within permissible limits, while also emphasizing the potential of inverter technologies to enhance the controllability, flexibility, and resilience of microgrids. In this context, the study supports the transition toward highly inverter-based, and ultimately fully inverter-based, power grids that can maximize the utilization of clean and sustainable energy resources. In addition, the developed simulation model provides a practical framework for studying, developing, and designing new microgrids, testing operational parameters and grid stability, and evaluating the integration of renewable energy sources into existing power systems under established operational scenarios. Overall, this simulation framework lays the groundwork for future research on advanced control strategies and real-time hardware-in-the-loop testing, thereby supporting the further development and deployment of inverter-based microgrids in practical power system environments and broader grid modernization initiatives.

REFERENCES

[1] Masenge I, Mwasilu F. (2020) Hybrid solar PV-wind generation system coordination control and optimization of battery energy storage system for rural electrification. In Proceedings of the 2020 IEEE PES/IAS PowerAfrica, 25-28 August 2020, Nairobi, Kenya

[2] Zeng J, Zhang B, Mao C, Wang Y. (2006) Use of battery energy storage system to improve the power quality and stability of wind farms. Proceedings of the 2006 International Conference on Power System Technology, 22-26 October 2006, Chongqing, China.

[3] Energy Transition Investment Trends 2025 [https://about.bnef.com]

[4] Renewables 2025 Global Status Report 2025 [https://www.ren21.net/gsr-2025]

[5] Grid-forming Inverter Market Size, Share & Trends Analysis Report 2023-2028 [https://www.skyquestt.com/report/grid-forming-inverter-market]

[6] U.S. Energy Storage Monitor: Q4 2024 [https://cleanpower.org/news/u-s-energy-storage-monitor-q4-2024]

[7] De Siqueira LMS, Peng W. (2021) Control strategy to smooth wind power output using battery energy storage system: A review. Journal of Energy Storage, 35:102252.

[8] Gao F, Iravani MR. (2008) A control strategy for a distributed generation unit in grid-connected and autonomous modes of operation. IEEE Transactions on Power Delivery, 23(2):850-9.

[9] Babu VV, Roselyn JP, Nithya C, Sundaravadivel P. (2024) Development of Grid-Forming and Grid-Following Inverter Control in Microgrid Network Ensuring Grid Stability and Frequency Response. Electronics, 13(10):1958.

[10] Rathnayake DB, Akrami M, Phurailatpam C, Me SP, Hadavi S, Jayasinghe G. (2021) Grid forming inverter modeling, control, and applications. IEEE Access, 9:114781-807.

[11] Uddin M, Mo H, Dong D, Elsawah S, Zhu J, Guerrero J. (2023) Microgrids: A review, outstanding issues and future trends. Energy Strategy Reviews, 49:101127.

[12] Roy P, He J, Zhao T, Singh Y. (2022) Recent advances of wind-solar hybrid renewable energy systems for power generation: a review. IEEE Open Journal of the Industrial Electronics Society, 3:81-104.

[13] Kafle L, Ni Z, Tonkoski R, Qiao Q. (2016) Frequency control of isolated micro-grid using a droop control approach. Proceedings of the 2016 IEEE International Conference on Electro Information Technology (EIT), Grand Forks, 19-21 May 2016, Grand Forks, ND, USA.

[14] Poonahela I, Krama A, Bayhan S, Fesli U, Shadmand MB, Abu-Rub H. (2023) Hierarchical model-predictive droop control for voltage and frequency restoration in AC microgrids. IEEE Open Journal of the Industrial Electronics Society, 4:85-97.

[15] Zulkifly Z, Yusoff SH, Tumeran NL, Razali NSI. (2023) Battery Energy Storage System (BESS) Modeling for Microgrid. IIUM Engineering Journal, 24(1):57-74.

[16] Li X, Hui D, Lai X. (2013) Battery energy storage station (BESS)-based smoothing control of photovoltaic (PV) and wind power generation fluctuations. IEEE Transactions on Sustainable Energy, 4(2):464-73.

[17] Chau TK, Yu SS, Fernando T, Iu HHC, Small M. (2019) An investigation of the impact of PV penetration and BESS capacity on islanded microgrids–a small-signal based analytical approach. Proceedings of the 2019 IEEE International Conference on Industrial Technology (ICIT), 13-15 February 2019, Melbourne, VIC, Australia.

[18] Anttila S, Döhler JS, Oliveira JG, Boström CJE. (2022) Grid forming inverters: A review of the state of the art of key elements for microgrid operation. Energies, 15(15):5517.

[19] Lamichhane R, Adhikari S. (2023) Virtual Synchronous Generator for Frequency Stability of Microgrid. Proceedings of the International Conference on Role of Energy for Sustainable Social Development; 14th-15th May 2023, Kathmandu, Nepal.

[20] Elwakil MM, El Zoghaby HM, Sharaf SM, Mosa MA. (2023) Adaptive virtual synchronous generator control using optimized bang-bang for Islanded microgrid stability improvement. Protection and Control of Modern Power Systems, 8(4):1-21.

[21] Chakraborty S, Patel S, Salapaka MV. (2022) µ-Synthesis-Based Generalized Robust Framework for Grid-Following and Grid-Forming Inverters. arXiv preprint arXiv:2207.02818. Available: https://arxiv.org/abs/2207.02818

[22] Lin Y, Zhu J, He F. (2025) An improved model-free predictive voltage control for grid-forming inverter with adaptive ultra-local data-model in renewable energy system. Frontiers in Energy Research, 13:1526992.

[23] Miller NW, Sanchez-Gasca JJ, Price WW, Delmerico RW. (2003) Dynamic modeling of GE 1.5 and 3.6 MW wind turbine-generators for stability simulations. Proceedings of the 2003 IEEE Power Engineering Society General Meeting (IEEE Cat No 03CH37491), 13-17 July 2003, Toronto, ON, Canada.

[24] Ngamroo I. (2017) Review of DFIG wind turbine impact on power system dynamic performances. IEEJ Transactions on Electrical Electronic Engineering, 12(3):301-11.

[25] Bossoufi B, Aroussi HA, Ziani E, Lagrioui A, Derouich A. (2014) Low-speed sensorless control of DFIG generators drive for wind turbines system. WSEAS Transactions on Systems and Control, 100:4.

[26] Hieu NH, Luu CT, Tuan TQ. (2015) Effects of DFIG wind power generation on Vietnam power system operation. Proceedings of the 2015 IEEE Eindhoven PowerTech, 29 June 2015 - 02 July 2015, Eindhoven, Netherlands.

[27] Khoa NM, Tung DD, Dai LV. (2022) Experimental study on low voltage ride-through of DFIG-based wind turbine. International Journal of Electrical Electronic Engineering Telecommunications, 11(1):1-11.

[28] Islam H, Mekhilef S, Shah NBM, Soon TK, Seyedmahmousian M, Horan B, Stojcevski A. (2018) Performance evaluation of maximum power point tracking approaches and photovoltaic systems. Energies, 11(2):365.

[29] Gao JT, Shih CH, Lee CW, Lo KY. (2022) An active and reactive power controller for battery energy storage system in microgrids. IEEE Access, 10:10490-9.